Generalized Continuum Theory for Nematic Elastomers: Non-affine Motion and Characteristic Behavior

Samuel C. Lamont[a], Franck J. Vernerey[a,*]

[a]*Department of Mechanical Engineering, University of Colorado Boulder, Boulder, 80303, USA*

Abstract

We develop a physically-motivated mechanical theory for predicting the behavior of nematic elastomers – a subset of liquid crystal elastomers (LCEs). We begin with a statistical description of network geometry that naturally incorporates independent descriptors for the mesogens, which create the nematic phase, and the polymer chains, which are assumed to not deform affinely with global deformations. From here, we develop thermodynamically consistent constitutive laws based on classical continuum mechanics principles and ultimately provide simple governing equations that have a transparent physical interpretation. We found that our framework converges identically to two previously developed mechanical theories, including the well-known neo-classical theory when considering the extreme ends of our parametric space. We then explore the new predictive capabilities of our model inside these two extremes and illustrate its unique predictions at finite strains, which are distinct in form from other theories. We validate our model using published experimental data from four monodomain nematic liquid crystal elastomers.

Keywords: Microstructures, Anisotropic material, Constitutive behavior, Non-affine motion, Nematic LCE

1. Introduction

Nematic elastomers, which feature mesogens in the nematic phase loosely cross-linked by flexible polymer chains, exhibit a rich variety of mechanical behaviors that are sometimes poorly understood. They are typically anisotropic, display phase transitions when exposed to a variety of stimuli, and are often celebrated for their excellent dissipation qualities. Nonetheless, these properties are quite volatile, and small changes in chemical design or synthesis may lead to a drastically different material. It is, thus, desirable to develop theoretical models that can connect design parameters to the mechanical behavior of the network.

In recent years, there has been an expansion of synthesis strategies for nematic elastomers, resulting in networks with widely diverse architectures and molecular interactions. For instance, chemists have designed materials with diverse mesogen-mesogen interactions for tuning the emergent properties (McCracken et al., 2021; Schlafmann et al.), as well as optimizing liquid crystal architecture for compatibility with 3D printing (Wang et al., 2020; Mistry et al., 2021). Perhaps the most notable new class of liquid crystal materials are those bonded with dynamic covalent or physical bonding (Pei et al., 2014; Saed et al., 2021), resulting in stronger viscoelastic response and higher processing abilities. These so-called "exchangeable" LCEs are akin to dynamic polymer networks, which typically behave as a viscous solid under certain loading conditions (Vernerey et al., 2017; Vernerey, 2022). With these developments in chemical architecture, the typical depiction of an ideal main-chain liquid crystal elastomer is becoming less common. It is unsurprising, then, that the mechanical behavior displayed by these new materials covers a broad spectrum of characteristic responses. Currently, there is a large push to connect the mechanical behavior of nematic elastomers to

*Corresponding author

Email addresses: samuel.lamont@colorado.edu (Samuel C. Lamont), franck.vernerey@colorado.edu (Franck J. Vernerey)

their chemical design for applications in 3D printing and artificial sensors (Saed et al., 2019; Ditter et al., 2020). To achieve this goal, more robust mechanical models must be developed with an emphasis on physical network descriptions and practical modeling parameters.

Perhaps the most prominent theoretical framework applied to nematic elastomers is the 'neo-classical' theory first presented in its general form in Bladon et al. (1993). The two most notable features of this model are that it directly embeds (i) the current state of nematic order and (ii) the inherent polymer chain anisotropy at its foundation. As a result, it can predict many features of nematic elastomers including the characteristic 'soft elastic' response. With this said, there is a diverse range of mechanical behaviors displayed by nematic elastomers, and the neo-classical theory does not predict a large family of responses without modifications (Mao et al., 1998). To account for these discrepancies, various extensions of the neo-classical theory have been proposed. Verwey and Warner (1997) introduced a notable extension of the neo-classical theory, in which, fluctuations in the chain population were accounted for to give rise to a 'semi-soft' response (Biggins et al., 2008). This and many other extensions and applications of the neo-classical theory are presented in detail in Warner and Terentjev (2007). Another important milestone in the development and understanding of the neo-classical theory was the quasi-convexification of the elastic energy density in the trace formula (DeSimone and Dolzmann, 2002; Conti et al., 2002). This allowed for finding the solution to boundary-value problems, which was used to predict patterning such as the stripe instability of LCEs. There has also been consistent development of alternative convex and quasi-convex free energy forms for nematic elastomers (DeSimone and Teresi, 2009), which have been used for analysis on patterned structures and instabilities frequently observed experimentally (Agostiniani and DeSimone, 2012).

Despite these significant developments, one fundamental assumption inherent to the neo-classical model is that the polymer chains deform *affinely* in space, that is, they follow the macroscopic deformation of the body. While this is a common assumption in simple flexible polymer networks such as some rubbers, it is known that topologically complex materials do not typically obey an affine deformation (Basu et al., 2011) at the lengthscale of the underlying polymer network (on the order of 1-10 nm). Furthermore, the non-affine motion of the mesogens is largely cited as the dominating factor for soft and semi-soft elastic behaviors, among others (Warner and Terentjev, 2007). A promising framework that can be used to address this coupling is the description of the nematic elastomer in the generalized continuum (Eringen, 1966). This may also be referred to as a 'micropolar' or 'micromorphic' formulation, which treats the nematic director field as an independent kinematic descriptor of the continuum. The most notable feature of these treatments is that the spatial gradients of the nematic field are naturally included in the formulation, which embeds a lengthscale directly into the constitutive developments, thereby connecting the liquid crystalline behavior of the mesogens to the mechanical behavior of the polymer network. Anderson et al. (1999) was the first to perform a rigorous thermodynamic study of these treatments in the context of nematic elastomers. More recently, Zhang et al. (2019) and Wang et al. (2022) used micropolar frameworks to study their time-dependent behaviors. With this said, the resulting formulations tend to be mathematically complex and difficult to use. Moreover, the physical depiction of the network is frequently lost, making it difficult to interpret the parameters in these models. To address this, our group previously proposed mechanical theories for transiently crosslinked highly aligned networks from a microstructural approach (Lalitha Sridhar and Vernerey, 2020; Vernerey, 2022). The elastic response, including instability and finite strain anisotropy, was not studied in detail as these works were focused on time-dependent behaviors. A microstructural study on the elastic response of nematic elastomers is still lacking, and needed, as the physical interpretation of modeling parameters is essential for effectively using a mechanical model to aid in the experimental design process.

In this work, we develop a new approach for predicting the mechanical behaviors of nematic elastomers. To depict a more general network architecture, we incorporate separate descriptions for the motion of the polymer chains and the mesogens, which places our theory into the family of generalized continuum theories. With this said, we maintain a microstructurally motivated depiction of the nematic elastomer by considering a single chain-mesogen unit and its statistically homogenized response. To better incorporate the lengthscale dependency that naturally arises from the generalized continuum approach, we consider that the motion of polymer chains in the network is non-affine. As a result, we describe nematic elastomers as a whole family of materials, in which, the soft polymer phase may have varying degrees of alignment with respect to the

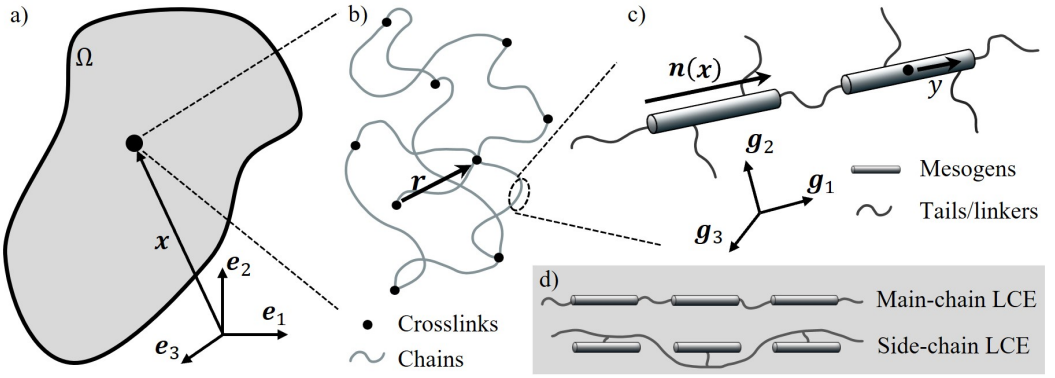

Figure 1: Depiction of the nematic elastomers studied in this paper. a) The domain Ω described by orthogonal basis $\{\boldsymbol{e}_i\}$, $1 \leq i \leq 3$. b) Schematic of the chains (grey lines) and crosslinking points (black dots) at a point $\boldsymbol{x} \in \Omega$. The end-to-end vector $\boldsymbol{r}$ is defined as spanning the distance between two crosslinks. c) Within a chain, the mesogens are described by the nematic director $\boldsymbol{n}(\boldsymbol{x})$, which defines a local coordinate system $\{\boldsymbol{g}_i\}$. The mesogen units (consisting of mesogen and aliphatic tail) are connected by flexible linkers that attach to the mesogens at a position y along their length. d) Illustrations of two typical LCE architectures, which have different distributions of y.

nematic liquid crystalline phase. The resulting formulation, therefore, generalizes the approach of Bladon et al. (1993), which will be shown to be a limiting case of the model under certain loading conditions. We illustrate the predictions of the model by comparing it to experimental data on monodomain nematic liquid crystal elastomers.

2. Statistical description of nematic elastomers

In soft nematic networks, flexible polymer chains coexist with stiff, rod-like mesogens to yield a material with one hybrid soft-and-stiff phase. The resulting mechanical behavior is drastically different from that of either phase alone and may be different from that of a more typical composite material as well. This is because coupled interactions between these phases are inherent to the microstructure and cannot be ignored. To account for this, we use a physical description of the material that accounts for each constituent and their naturally arising interactions at its foundation. The resulting formulation is that of a simplified general continuum with only three physically-motivated fitting parameters.

2.1. Continuum description of a nematic elastomer

Let us consider a typical nematic elastomer consisting of rod-like mesogens linked by flexible polymer chains. The network exists in a region $\Omega \subset \mathbb{R}^3$ defined by the orthogonal set of basis vectors $\{\boldsymbol{e}_i\}$, $1 \leq i \leq 3$ (Fig. 1a). At each position $\boldsymbol{x} \in \Omega$, there exists a population of polymer chains connected by crosslinking junctions. We use $\boldsymbol{r}$ to denote the end-to-end vector of a chain spanning two crosslinking junctions (Fig. 1b). Within a chain, the single mesogen 'unit' may be isolated as depicted in Fig. 1c. This unit consists of the rigid mesogen core, an aliphatic tail, and any spacers or linkers (Herbert et al., 2022). In the nematic phase, each mesogen is considered to be oriented along a consistent direction. We thus use the field variable $\boldsymbol{n}(\boldsymbol{x})$ to describe the vector spanning a single mesogen, which is assumed to be consistent for all mesogens located at a specific position $\boldsymbol{x} \in \Omega$. To facilitate our thermodynamic approach, the mesogens themselves are considered to have initial length ℓ_0 and current length ℓ, such that the stretch ratio $\lambda^*(\boldsymbol{x}) = \ell/\ell_0$ describes the change in length for an $\boldsymbol{n}(\boldsymbol{x})$ with initial value $\boldsymbol{n}_0(\boldsymbol{x})$. We then treat $\boldsymbol{n}$ as a dimensionless quantity parameterized by the stretch ratio λ^* and current nematic director orientation $\boldsymbol{g}_1$ such that

$$\boldsymbol{n} = \lambda^* \boldsymbol{g}_1, \tag{1}$$

with the requirement $\boldsymbol{g}_1 \cdot \boldsymbol{g}_1 = 1$. Note that in most nematic elastomers, the mesogen is rigid and will not change its length. This will be accounted for when defining the energetic quantities in the system. For

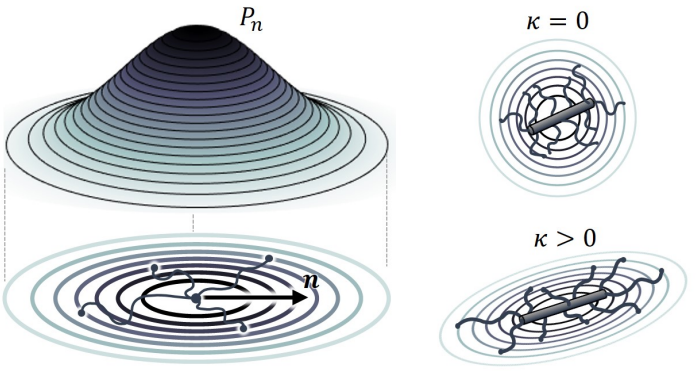

Figure 2: The natural conformation P_n at a point $\boldsymbol{x} \in \Omega$ with nematic director $\boldsymbol{n}(\boldsymbol{x})$. The chain bias κ is illustrated to deform the reference distribution such that it is transversely isotropic about $\boldsymbol{n}$. In the limiting case of $\kappa = 0$, the distribution of end-to-end vectors is isotropic, even though the mesogens remain in perfect nematic alignment.

generality, we assume that the mesogens may be linked at any position y along their length, which we will for now treat as a known variable that depends on the LCE architecture (main-chain, side-chain, etc.) as depicted in Fig. 1d. Moreover, while $\boldsymbol{n}$ is considered to be perfectly nematic (such that there is negligible variance in $\boldsymbol{n}$ at a point $\boldsymbol{x}$), the end-to-end vectors $\boldsymbol{r}$ follow a statistical distribution $P(\boldsymbol{r};\ \boldsymbol{x})$ due to their entropic motion in space. Here, the semicolon is used to separate the statistical variable $\boldsymbol{r}$ from the spatial coordinate variable $\boldsymbol{x}$. With this description, the current network geometry may be inferred by the effective step lengths $r_\parallel$ in the direction of $\boldsymbol{n}$ and $r_\perp$ in the orthogonal directions. Formally, these quantities are defined in a statistical sense as

$$\langle r_\parallel^2 \rangle = \int P(\boldsymbol{r})\,(\boldsymbol{r}\cdot\boldsymbol{g}_1)^2\,d\Omega_r, \qquad \langle r_\perp^2 \rangle = \int P(\boldsymbol{r})\,(\boldsymbol{r}\cdot\boldsymbol{g}_2)^2\,d\Omega_r, \tag{2}$$

where integration is performed over the conformation space Ω_r of P and $\boldsymbol{g}_2$ is the in-plane orthogonal direction (Fig. 1c). This theory is concerned with following the distribution $P(\boldsymbol{r};\ \boldsymbol{x})$ and the nematic director $\boldsymbol{n}(\boldsymbol{x})$ for arbitrary deformations of Ω.

2.2. Polymer Conformation

We now turn to the question of describing the conformation of the polymer chains described by the distribution $P(\boldsymbol{r};\ \boldsymbol{x})$. While the orientation of the mesogen is completely determined by the director $\boldsymbol{g}_1$, the polymer chains are randomly oriented in space due to the influence of thermal noise and entropic motion (see Doi (2013), for instance). The orientation of a chain may be correlated with the director $\boldsymbol{g}_1$, however, and it may also be influenced by the connectivity of the mesogen units via their location y of attachment (Vernerey, 2022). We therefore postulate the existence of a *natural* conformation $P_n(\boldsymbol{r};\ \boldsymbol{x})$ of chains, which describes the preferred conformation of $\boldsymbol{r}$ at a position $\boldsymbol{x} \in \Omega$. In contrast to networks of flexible chains, this may be biased to favor alignment or dis-alignment with the nematic director $\boldsymbol{n}(\boldsymbol{x})$ depending on their preferred packing and polarity (Warner and Terentjev, 2007). Let us postulate that, in their natural state, each chain is uniformly biased by the nematic director. In this case, we may express $P_n(\boldsymbol{r};\ \boldsymbol{x})$ as a field variable that only depends on $\boldsymbol{n}(\boldsymbol{x})$ at a specific point $\boldsymbol{x} \in \Omega$. We consider such a point $\bar{\boldsymbol{x}} \in \Omega$ and postulate that its natural conformation $\bar{P}_n(\boldsymbol{r}) = P_n(\boldsymbol{r};\ \bar{\boldsymbol{x}})$ may be generally expressed as a biased Gaussian distribution of the form

$$\bar{P}_n(\boldsymbol{r}) = \left[\left(\frac{1}{2\pi r_0^2}\right)^3 \frac{1}{\mathrm{Det}\bar{\boldsymbol{\mu}}}\right]^{1/2} \exp\left(-\frac{1}{r_0^2}\boldsymbol{r}\cdot\bar{\boldsymbol{\mu}}^{-1}\cdot\boldsymbol{r}\right), \tag{3}$$

where the conformation bias tensor $\bar{\boldsymbol{\mu}}$ represents the tendency for chains to assume a non-isotropic configuration due to the influence of the mesogens and r_0^2 is the mean squared end-to-end distance of a polymer chain in its resting configuration. In this theory, we take r_0^2 to be constant, regardless of the degree of bias

induced by the mesogen. In other words, the mesogens only influence the resting anisotropy or orientation of the polymer chains and not their average resting length. Let us consider that the polymer chains tend to achieve a transversely isotropic distribution about the nematic director $\bar{\boldsymbol{g}}_1 = \boldsymbol{g}_1(\bar{\boldsymbol{x}})$. In this case, the bias tensor $\bar{\boldsymbol{\mu}}$ may be generally written as

$$\bar{\boldsymbol{\mu}} = (1-\kappa)\,\boldsymbol{I} + 3\kappa\,(\bar{\boldsymbol{g}}_1 \otimes \bar{\boldsymbol{g}}_1)\,, \tag{4}$$

where $\otimes$ denotes the dyadic (tensor) product and κ is a scalar parameter that describes the degree of alignment. It varies between $\kappa = 0$ when the material is fully isotropic and $\kappa = 1$ when the chains are perfectly in line with the rods (Fig. 2). In general, κ may also be negative (up to $\kappa = -1/2$), which implies a preferred packing of polymer chains orthogonal to the mesogens. With this said, in Eq. (4), notice that $\mathrm{Tr}\bar{\boldsymbol{\mu}} \equiv 3$ is independent of κ, which reflects our assumption that r_0^2 is constant. Physically, κ represents the normalized ratio of effective step lengths $r_\parallel$ and $r_\perp$ in the parallel and perpendicular directions, respectively. This is similar to the neo-classical distribution of chains described in Bladon et al. (1993), but we note that we are not considering the mesogen as part of the effective 'chain.' Instead, we are strictly defining the natural conformation of chains in the polymer network independently for all $\boldsymbol{x} \in \Omega$. Alternatively, this may be interpreted as the chain conformation distribution $P(\boldsymbol{r};\ \boldsymbol{x})$ that would be achieved at a position $\boldsymbol{x} \in \Omega$ if the material were allowed to relax while holding the current nematic director orientation $\boldsymbol{g}_1$ constant. We, thus, prefer the term *natural* conformation as opposed to *reference* conformation as $P_n(\boldsymbol{r};\ \boldsymbol{x})$ evolves with the nematic director field. As illustrated later, this provides more flexibility in the system's kinematics as the motion of the rods and the polymer network may be considered in isolation.

2.3. Non-affine crosslinker motion

We now turn to the question of describing the motion of $\boldsymbol{n}$ and $\boldsymbol{r}$ at a given position $\boldsymbol{x} \in \Omega$. While $\boldsymbol{n}$ will be treated as its own kinematic field variable, an explicit definition of the motion of $\boldsymbol{r}$ relies on a kinematic assumption regarding the motion of the polymer network within the nematic system. From a continuum standpoint, this may be formally expressed using the deformation gradient $\boldsymbol{F} = \partial\boldsymbol{x}/\partial\boldsymbol{X}$, which maps the motion of an elementary volume initially located at a position $\boldsymbol{X} \in \Omega_0$ of the reference configuration to its current position $\boldsymbol{x} \in \Omega$.

As the rotation of the mesogen may not follow that of the global deformation, we do not expect the motion of the microstructure at a point $\boldsymbol{x} \in \Omega$ to be affine (i.e., quantities located at $\boldsymbol{x}$ do not deform exactly with $\boldsymbol{F}$). In a previous work (Vernerey, 2022), we studied a system in which the convex hull of an elementary volume deforms affinely, but the motion of points within the hull does not. In this study, we consider a more generalized assumption regarding the nature of non-affine motion in the network. Let us note that the motion of an end-to-end vector $\boldsymbol{r}$ with initial value $\boldsymbol{r}_0$ may be generally decomposed into an affine part and a non-affine part such that $\boldsymbol{r} = \boldsymbol{F}\cdot\boldsymbol{r}_0 + \boldsymbol{r}_{na}$, where $\boldsymbol{r}_{na}$ is the non-affine part of $\boldsymbol{r}$. As the end-to-end vector consists of a linear sum of the vector spanning each mesogen unit within the chain, it is reasonable to conclude that $\boldsymbol{r}_{na}$ is a function of the mesogen motion $\boldsymbol{n}$. The simplest kinematic assumption to link these two quantities is that the non-affine part of $\boldsymbol{r}$ is proportional to the non-affine part of $\boldsymbol{n}$. Thus, we propose the following evolution law:

$$\boldsymbol{r} = \boldsymbol{F}\cdot\boldsymbol{r}_0 + \gamma\ell_0\,(\boldsymbol{n} - \boldsymbol{F}\cdot\boldsymbol{n}_0)\,, \tag{5}$$

where γ is a scalar coefficient that dictates the strength of the non-affinity. In the case of $\gamma = 0$, the motion of $\boldsymbol{r}$ is perfectly affine. Large values of γ would tend to align the rotation of the mesogens with that of the polymer chains. It may also be noted that in the case of affine mesogen motion, $\boldsymbol{n} = \boldsymbol{F}\cdot\boldsymbol{n}_0$ and the term on the right vanishes, which enforces that the motion of $\boldsymbol{r}$ is also affine. As it stands, γ will just be taken as an arbitrary coefficient. Its possible physical interpretations are discussed in the next section after a homogenized depiction of the network geometry is established.

2.4. Reduced Statistical description

In this study, we are concerned with the motion and reorientation of the nematic network when a macroscopic deformation is applied to the body. For the polymer network, this equates to tracking the

current chain distribution $P(\boldsymbol{r};\ \boldsymbol{x})$ as it is perturbed from some initial configuration P_0. Note that the initial distribution P_0 is only equal to the natural conformation distribution P_n if there has not been a change in the director orientation (or if $\kappa = 0$ and the network is isotropic). To create a more concise description of the network, we may consider that the thermodynamic quantities associated with deforming the network only depend on the statistical moments of $P(\boldsymbol{r};\ \boldsymbol{x})$, which greatly reduces the complexity of the problem. This is equivalent to a mean-field statistical assumption, which is exactly accurate for linear (Gaussian) chain statistics and is a valid assumption for certain regimes of non-linear statistics (Vernerey, 2018). A homogenized kinematic description is then established by defining the following second-order tensors:

$$\boldsymbol{\mu} = \frac{1}{r_0^2}\langle \boldsymbol{r} \otimes \boldsymbol{r} \rangle, \qquad \boldsymbol{\eta} = \frac{\gamma \ell_0}{r_0^2}\langle \boldsymbol{r} \otimes \boldsymbol{n} \rangle, \qquad \boldsymbol{\rho} = \boldsymbol{n} \otimes \boldsymbol{n}, \tag{6}$$

where brackets $\langle \cdot \rangle$ indicate the statistical averaging procedure defined in Eq. (2). The prefactors in front of $\boldsymbol{\mu}$ and $\boldsymbol{\eta}$ are added to non-dimensionalize them in a convenient form. Note that while these quantities are also field variables defined for $\boldsymbol{x} \in \Omega$, we have omitted the arguments for brevity. In the remainder of this manuscript, we denote these three quantities as *conformation tensors*, as they embed information regarding the current state of conformation of the chains and mesogens (see Vernerey et al. (2017) and Vernerey (2022) for further discussion). Briefly, the first tensor, $\boldsymbol{\mu}$, is an Eulerian strain-like quantity, akin to the left Cauchy-Green tensor of a classical continuum. It characterizes the conformation of polymer chains according to their average stretch and principal directions of deformation. The second tensor, $\boldsymbol{\eta}$, is a coupled tensor that represents strains of the chain with respect to the mesogens, and vice-versa. We may better understand $\boldsymbol{\eta}$ by looking into its components. Let us first note that the director orientation $\boldsymbol{g}_1$ and its in-plane and out-of-plane orthogonal vectors $\boldsymbol{g}_2$ and $\boldsymbol{g}_3$ form an orthogonal basis centered about the mesogen orientation. In general, we may decompose any second-rank tensor $\boldsymbol{A}$ as

$$\boldsymbol{A} = A_{ij}\boldsymbol{g}_i \otimes \boldsymbol{g}_j, \tag{7}$$

where repetition is implied over repeated subscripts. In Eq. (7), the quantities $A_{ij} = \boldsymbol{A} : \boldsymbol{g}_i \otimes \boldsymbol{g}_j$ are the components of $\boldsymbol{A}$ in the $\boldsymbol{g}_i \otimes \boldsymbol{g}_j$ basis. Due to its definition, the decomposition of $\boldsymbol{\eta}$ becomes

$$\boldsymbol{\eta} = \eta_{11}\boldsymbol{g}_{11} + \eta_{21}\boldsymbol{g}_{21} + \eta_{31}\boldsymbol{g}_{31}, \tag{8}$$

where the shorthand $\boldsymbol{g}_{ij} = \boldsymbol{g}_i \otimes \boldsymbol{g}_j$ was adopted. Thus, $\boldsymbol{\eta}$ has only three degrees of freedom: one parallel to the mesogen and two perpendicular in-plane and out-of-plane, respectively. Each component describes a physical competition between the stretch of the mesogens and the stretch of the polymer chains. The parallel component tends to stretch or compress the mesogen, while the perpendicular components tend to rotate it (Fig. 3). We also note that, due to its definition, $\boldsymbol{\eta}$ is zero whenever $P(\boldsymbol{r};\ \boldsymbol{x})$ is zero, which is true when the network is at rest, requiring that the initial value $\boldsymbol{\eta}_0 = \boldsymbol{0}$. The final tensor, $\boldsymbol{\rho}$, is also a strain-like tensor that characterizes the stretch and orientation of the mesogens. Note that in the nematic system, $\boldsymbol{n}$ is not a random variable, and thus neither is $\boldsymbol{\rho}$. Due to this, we may express the following identities:

$$\boldsymbol{\rho} = (\lambda^*)^2 \boldsymbol{g}_{11}, \qquad \boldsymbol{\rho}_0 = \boldsymbol{n}_0 \otimes \boldsymbol{n}_0, \tag{9}$$

where $\boldsymbol{\rho}_0$ is the initial value of $\boldsymbol{\rho}$. The useful identity that $\mathrm{Tr}\boldsymbol{\rho} = (\lambda^*)^2$ will be useful in solving for the stretch λ^* and orientation $\boldsymbol{g}_1$ independently. Having defined the kinematic evolution of $\boldsymbol{r}$ in Eq. (5), we may now use the definition of the remaining conformation tensors in Eq. (6) to express them explicitly in terms of $\boldsymbol{F}$ and $\boldsymbol{n}$. After some simple algebra, the solutions are written

$$\boldsymbol{\mu} = \boldsymbol{F} \cdot (\boldsymbol{\mu}_0 + \chi\boldsymbol{\rho}_0) \cdot \boldsymbol{F}^T - \left(\boldsymbol{\eta} + \boldsymbol{\eta}^T\right) - \chi\boldsymbol{\rho}, \tag{10}$$

$$\boldsymbol{\eta} = \chi\left[\boldsymbol{F} \cdot (\boldsymbol{n}_0 \otimes \boldsymbol{n}) - \boldsymbol{\rho}\right], \tag{11}$$

where $\boldsymbol{\mu}_0$ is the initial value of $\boldsymbol{\mu}$ and we defined the normalized rotational inertia χ of mesogen to be:

$$\chi = \left(\frac{\gamma \ell_0}{r_0}\right)^2. \tag{12}$$

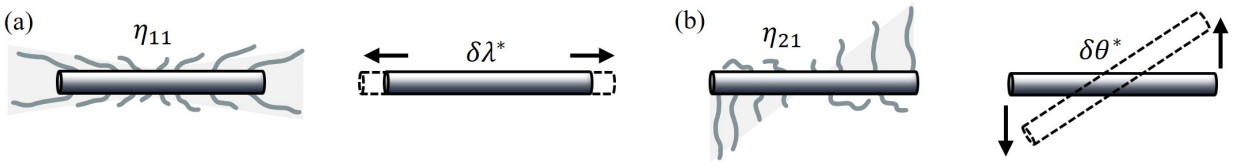

Figure 3: Illustration of the components of $\boldsymbol{\eta}$ and the resulting mesogen deformations. Polymer chains are placed along the mesogens for illustrative purposes.

The dimensionless parameter χ naturally arrives from the derivation (see Appendix 8.1 and Vernerey (2022)) and will be shown to greatly affect the response of the system. It is not insignificant that $\boldsymbol{\mu}$ and $\boldsymbol{\eta}$ may be expressed entirely using the normalized quantity χ, such that γ, ℓ_0, and r_0 do not appear independently in these equations. The kinematics of the system, and as a result, its elastic energy density, may thus be parameterized using only χ. As it may be interpreted as contributing to the "microinertia" of a generalized continuum (Eringen, 1966), we will simply refer to χ as "rotational microinertia" in the remainder of the manuscript for brevity. Equations (10) – (12) conclude the kinematic description of our model. Thus, given an applied macroscopic deformation gradient $\boldsymbol{F}$ and nematic director field $\boldsymbol{n}$, the chain conformation, rod conformation, and coupled strain of the system can be determined.

2.4.1. On the non-affine proportionality coefficient γ

We here dedicate a brief discussion to the proportionality coefficient γ. While the degree of non-affine motion of $\boldsymbol{r}$ is dictated by γ, the homogenized statistical moments of $P(\boldsymbol{r};\ \boldsymbol{x})$ are only functions of the rotational microinertia χ. Thus, the ratio $\gamma\ell_0/r_0$, which is expressed in terms of the lengthscale r_0 of the polymer chains and the lengthscale $\gamma\ell_0$ of non-affine motion, is more indicative of the behavior of the system. This leaves us with only one kinematic fitting parameter but proposes the question of how to determine γ for a system with a known physical architecture. In this context, we may postulate that γ should be related to the position y at which neighboring mesogens are linked (Fig. 1c). In main-chain LCEs, this position is at a consistent spacing $y = \ell_0/2$ from the centerpoint of the mesogen. If there are N repeating mesogen units along the chain, then the factor $\gamma = N/2$ would reflect the assumption that the convex hull between neighboring mesogens is assumed to deform affinely. Similarly, if the approximate attachment location is known for a side-chain LCE architecture, $\gamma = fN$ would maintain the same assumption, where f is the fractional attachment location along the length of the mesogen.

An alternative depiction was studied in a previous manuscript (Vernerey, 2022), which considered that y is itself a statistical variable that may take any position along the mesogen within a particular polymer chain. This would be more reminiscent of biopolymers such as the actin cortex that, while not fitting under the standard definition of a liquid crystal elastomer, do feature highly aligned architectures and display similar behaviors including soft modes of elasticity (Dalhaimer et al., 2007). In this case, we determined the proportionality coefficient to be $\gamma = \sqrt{12}$ based on a statistical definition of the second moment of the mesogens about their linkage points (Vernerey, 2022). In this case, it was assumed that the lengthscale of the aligned units could be on the order of the lengthscale of the crosslinking junctions, which is not the case for LCEs. Nonetheless, the previous statistical definition of χ as a normalized rotational moment motivates our description here of χ as reflecting the microinertia of the system.

3. Energy and governing equations

We now complete the thermodynamic description of our system by considering the work done by an external deformation and applying the conservation laws of continuum thermodynamics. In a first-order continuum formulation, the free energy density ψ per unit volume is expressed in terms of the field variables $\boldsymbol{x}$ and $\boldsymbol{n}$ as well as their spatial gradients. We thus consider a general framework by which we define the kinematic descriptors of the continuum and subsequently define energetic conjugates with which they expend power (Anand, 2012; Gil et al., 2022). In place of explicitly stating the balances of linear and

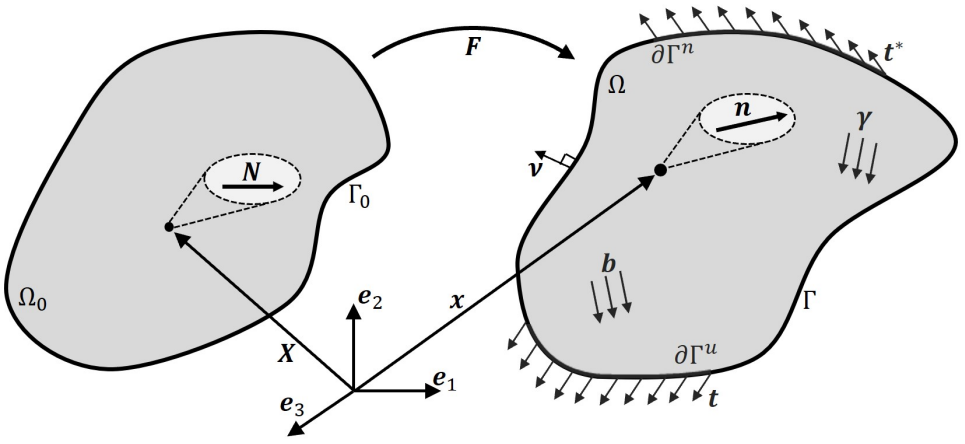

Figure 4: The motion of Ω from its reference configuration Ω_0 with external loads labeled.

angular momenta, we invoke the principles of frame invariance and virtual power, which will be shown to yield equivalent governing equations for the system. To avoid lengthy derivations, we minimize the number of thermodynamic quantities defined to only those relevant to the current study. For rigorous discussion on the continuum thermodynamics of multi-field or higher-order continua, we refer the reader to Eringen (1999), Germain (1973), and Anderson et al. (1999). Moreover, we consider our system to be in quasi-static equilibrium for all motions and, thus, neglect inertial terms in the following derivations.

3.1. Frame invariance and virtual power

We consider an Eulerian presentation of the continuum, taking place in the current configuration Ω, which has been deformed from its reference configuration $\Omega_0 \subset \mathbb{R}^3$ (Fig. 4). The boundary $\Gamma = \partial\Omega$ is oriented by a unit normal field $\boldsymbol{\nu}$ directed outward from Ω. For all $\boldsymbol{x} \in \Omega$, we consider the following set of kinematic descriptors:

$$\mathcal{K} = \{\dot{\boldsymbol{x}}, \boldsymbol{\ell}, \dot{\boldsymbol{n}}, \boldsymbol{\xi}\}, \quad \text{with} \quad \boldsymbol{\ell} \equiv \nabla\dot{\boldsymbol{x}} \ \text{ and } \ \boldsymbol{\xi} \equiv \nabla\dot{\boldsymbol{n}}, \tag{13}$$

which is made from the kinematic variables present in our system. Note that $\nabla = \partial/\partial\boldsymbol{x}$ denotes the spatial gradient operator and $\boldsymbol{\ell}$ is the typical Eulerian velocity gradient. Similarly, $\boldsymbol{\xi}$ is the spatial gradient of the rate of mesogen deformation (akin to the micro-velocity gradient of higher-order continua). The rate $\mathcal{P}_{int}$ of internal power expenditure may be generally expressed in terms of energetically conjugate variables to these kinematic descriptors as

$$\mathcal{P}_{int} = \int_\Omega \left[\boldsymbol{h}\cdot\dot{\boldsymbol{x}} + \boldsymbol{\sigma} : \boldsymbol{\ell} + \boldsymbol{\pi}\cdot\dot{\boldsymbol{n}} + \boldsymbol{\Sigma} : \boldsymbol{\xi}\right] dv, \tag{14}$$

where $\boldsymbol{h}, \boldsymbol{\sigma}, \boldsymbol{\pi}$ and $\boldsymbol{\Sigma}$ are internal field variables that act as conjugates to $\dot{\boldsymbol{x}}, \boldsymbol{\ell}, \dot{\boldsymbol{n}}$, and $\boldsymbol{\xi}$, respectively. Their physical meaning will become clear in the subsequent derivations. To maintain simplicity, in this theory, we only consider external quantities conjugate to the independent field variables (and not their gradients). Thus, we may generally express the external power expenditure as

$$\mathcal{P}_{ext} = \int_\Omega \left[\boldsymbol{b}\cdot\dot{\boldsymbol{x}} + \boldsymbol{\gamma}\cdot\dot{\boldsymbol{n}}\right] dv + \int_\Gamma \left[\boldsymbol{t}^u(\boldsymbol{\nu})\cdot\dot{\boldsymbol{x}} + \boldsymbol{t}^n(\boldsymbol{\nu})\cdot\dot{\boldsymbol{n}}\right] da, \tag{15}$$

where $\boldsymbol{b}$ is a body force per unit volume that expends power with $\dot{\boldsymbol{x}}$ and $\boldsymbol{\gamma}$ is a body couple per unit volume that expends power with $\dot{\boldsymbol{n}}$. Similarly, $\boldsymbol{t}^u(\boldsymbol{\nu})$ is the force-traction that acts over $\dot{\boldsymbol{x}} \in \Gamma$ and $\boldsymbol{t}^n(\boldsymbol{\nu})$ is the corresponding moment-traction acting over $\dot{\boldsymbol{n}} \in \Gamma$.

Principle of frame indifference. Let us begin constraining the thermodynamic state of the system by asserting the principle of frame indifference, which states that, for any change in the current frame, the internal energy must remain unchanged. We may thus consider the equivalence of the quantities

$$\mathcal{P}_{int}\left(\mathcal{K}\right) = \mathcal{P}_{int}\left(\mathcal{K}^{*}\right), \tag{16}$$

where the superscript $()^{*}$ denotes the image in a new frame. We may generally express each quantity in a new frame using a proper orthogonal tensor $\boldsymbol{Q}$ and an arbitrary translation vector $\boldsymbol{a}$ such that $\dot{\boldsymbol{x}} = \boldsymbol{Q}\cdot\dot{\boldsymbol{x}}+\dot{\boldsymbol{Q}}\cdot\boldsymbol{x}+\dot{\boldsymbol{a}}$ and $\dot{\boldsymbol{n}} = \boldsymbol{Q}\cdot\dot{\boldsymbol{n}} + \dot{\boldsymbol{Q}}\cdot\boldsymbol{n}$. The definitions of their gradients in the new frame immediately follow. From here, we set $\mathcal{P}_{int}\left(\mathcal{K}\right) = \mathcal{P}_{int}\left(\mathcal{K}^{*}\right)$ and, after a lengthy derivation in Appendix 8.2, end up with the following requirement for satisfying frame invariance:

$$\boldsymbol{\sigma} + \boldsymbol{\beta} + \boldsymbol{\Sigma}\cdot\left(\nabla\boldsymbol{n}\right)^{T} = \boldsymbol{\sigma}^{T} + \boldsymbol{\beta}^{T} + \nabla\boldsymbol{n}\cdot\boldsymbol{\Sigma}^{T}, \tag{17}$$

where we defined the resultant moment tensor $\boldsymbol{\beta} = \boldsymbol{\pi}\otimes\boldsymbol{n}$ as the natural tensor that arises from the resultant moment $\boldsymbol{\pi}$. Note that in the absence of the nematic field $\boldsymbol{n}(\boldsymbol{x})$, Eq. (17) recovers the familiar expression $\boldsymbol{\sigma} = \boldsymbol{\sigma}^{T}$, which resembles the balance of angular momentum for a classical continuum. Thus, we may interpret $\boldsymbol{\sigma}$ as the Cauchy stress tensor and $\boldsymbol{\Sigma}$ as its micro-counterpart. With this said, it is important to recall that $\boldsymbol{\Sigma}$ is physically a torque per unit area due to its conjugacy to $\boldsymbol{\xi}$. For this reason, $\boldsymbol{\Sigma}$ is typically referred to as the couple-stress tensor.

Principle of virtual power. We next enforce the equivalence of virtual powers in the system. For any arbitrary realization of the fields in $\mathcal{K}$, we require that

$$\mathcal{P}_{int}(\mathcal{K}) = \mathcal{P}_{ext}(\mathcal{K}). \tag{18}$$

Using Eqs. (14) and (15), we perform an integration by parts and and express the principle of virtual power as

$$\begin{aligned}\int_{\Omega}\Big[\left(\boldsymbol{\pi}-\boldsymbol{\gamma}-\nabla\cdot\boldsymbol{\Sigma}\right)\cdot\dot{\boldsymbol{n}} - \left(\nabla\cdot\boldsymbol{\sigma}+\boldsymbol{b}\right)\cdot\dot{\boldsymbol{x}}\Big]dv + ... \\ ... + \int_{\Gamma}\Big[\left[\boldsymbol{\sigma}\cdot\boldsymbol{\nu}-\boldsymbol{t}^{u}(\boldsymbol{\nu})\right]\cdot\dot{\boldsymbol{x}} + \left[\boldsymbol{\Sigma}\cdot\boldsymbol{\nu}-\boldsymbol{t}^{n}(\boldsymbol{\nu})\right]\cdot\dot{\boldsymbol{n}}\Big]da = 0.\end{aligned} \tag{19}$$

As this expression must vanish for arbitrary $\dot{\boldsymbol{x}}$ and $\dot{\boldsymbol{n}}$ inside of Ω and on Γ, we obtain the localized balance laws

$$\begin{aligned}\nabla\cdot\boldsymbol{\sigma}+\boldsymbol{b} &= \boldsymbol{0}, \\ \nabla\cdot\boldsymbol{\Sigma}+\boldsymbol{\gamma}-\boldsymbol{\pi} &= \boldsymbol{0},\end{aligned} \tag{20}$$

as well as the traction conditions

$$\begin{aligned}\boldsymbol{t}^{u}(\boldsymbol{\nu}) &= \boldsymbol{\sigma}\cdot\boldsymbol{\nu}, \\ \boldsymbol{t}^{n}(\boldsymbol{\nu}) &= \boldsymbol{\Sigma}\cdot\boldsymbol{\nu}.\end{aligned} \tag{21}$$

We recognize the first equation in Eq. (20) as the balance of linear momentum in the classical continuum and $\boldsymbol{b}$ as the typical body force per unit volume. The second equation in Eq. (20) may be thought of as akin to a micro-balance of linear momentum, but note that both the body couple $\boldsymbol{\gamma}$ and the resultant moment $\boldsymbol{\pi}$ appear in the balance. While the external body couple $\boldsymbol{\gamma}$ may be considered to originate from an applied field tending to rotate the mesogens (such as a magnetic field), the resultant moment $\boldsymbol{\pi}$ is the resultant of the forces applied by the chains onto the mesogens. It is, thus, an internal moment originating from the coupled interactions of the chains and mesogens.

3.2. Balance of mechanical energy

We next consider the transfer of energy within the nematic system from an external deformation or applied stress. We begin by considering the elastic energy density ψ per unit volume, which may contain contributions due to stretching the polymer network as well as stretching the mesogens. We may leverage our statistical description of the system and claim that the energy density is only a function of the conformation tensors $\boldsymbol{\mu}, \boldsymbol{\eta}$, $\boldsymbol{\rho}$, and their gradients. To simplify the exposition (and noting that we will eventually not consider any gradient terms), we here only consider general energy dependency on the gradient $\nabla \boldsymbol{n}$ of the director field instead of the gradient of the director tensor $\boldsymbol{\rho}$. Moreover, we note that the simplest description of the network may be achieved with only $\boldsymbol{\mu}$ and $\boldsymbol{\rho}$ as the couple tensor $\boldsymbol{\eta}$ is included in the definition of $\boldsymbol{\mu}$ (see Eq. (10)). We, therefore, begin by defining a general energy functional $\psi(\boldsymbol{\mu}, \boldsymbol{\rho}, \nabla \boldsymbol{n})$ and evaluate its thermodynamic implications in terms of energy conjugacy with the velocity gradient $\boldsymbol{\ell}$ and the director field $\boldsymbol{n}$. Let us directly write the local form of the Clausius-Duhem inequality as

$$\boldsymbol{\sigma} : \boldsymbol{\ell} + \boldsymbol{\pi} \cdot \dot{\boldsymbol{n}} + \boldsymbol{\Sigma} : \boldsymbol{\xi} - \dot{\psi} \geq 0. \tag{22}$$

In an elastic system, the inequality vanishes identically as all processes are energy-conserving. Using the standard Coleman-Noll procedure, the Cauchy stress $\boldsymbol{\sigma}$, resultant moment tensor $\boldsymbol{\beta}$, and couple-stress $\boldsymbol{\Sigma}$ may be generally expressed as

$$\boldsymbol{\sigma} = 2 \left[\frac{\partial \psi}{\partial \boldsymbol{\mu}} \cdot (\boldsymbol{\mu} + \boldsymbol{\eta}) \right], \tag{23}$$

$$\boldsymbol{\beta} = 2 \left[\frac{\partial \psi}{\partial \boldsymbol{\rho}} \cdot \boldsymbol{\rho} - \frac{\partial \psi}{\partial \boldsymbol{\mu}} \cdot \boldsymbol{\eta} \right], \tag{24}$$

$$\boldsymbol{\Sigma} = \frac{\partial \psi}{\partial \nabla \boldsymbol{n}}. \tag{25}$$

The resultant moment tensor $\boldsymbol{\beta}$ may, thus, be conveniently expressed in terms of the conformation tensors we have defined. For the interested reader, we provide a derivation of Eqs. (22) – (25) in Appendix 8.3.

3.3. Free Energy of a Gaussian Nematic

We next consider a particular form of the energy functional ψ as informed by our kinematic description of the system. As described previously, the networks considered in this work store elastic energy in two ways: (a) the entropic stretch of the cross-linkers, described by the conformation tensor $\boldsymbol{\mu}$, and (b) the enthalpic stretch of the mesogen, captured by the tensor $\boldsymbol{\rho}$. In subsequent analysis, we will assume a homogeneous deformation of the body such that the gradient term $\nabla \boldsymbol{n}$ and its associated couple-stress $\boldsymbol{\Sigma}$ vanish for all deformations. Let us, then, consider a decomposition of $\psi(\boldsymbol{\mu}, \boldsymbol{\rho})$ into the following components:

$$\psi(\boldsymbol{\mu}, \boldsymbol{\rho}) = \psi_c(\boldsymbol{\mu}) + \psi_m(\boldsymbol{\rho}) + \psi_J(J), \tag{26}$$

where ψ_c is the energy density of the polymer matrix, ψ_m is the enthalpic energy density associated with stretching the mesogens, and ψ_J expresses bulk resistance to volume change given by $J = \det \boldsymbol{F}$. For this study, let us assume that the mesogens are sufficiently rigid such that they will not be stretched and that the material is globally highly incompressible. In this case, the energy densities ψ_m and ψ_J may be written as convex penalty functions to enforce that $\mathrm{Tr}\boldsymbol{\rho} = (\lambda^*)^2 = 1$ and $J = 1$. The remaining energy density ψ_c is derived from the Gaussian chain assumption of an anisotropic polymer (see Bladon et al. (1993) or Warner and Terentjev (2007)) and may be written as

$$\psi_c = \frac{G}{2} \left(\mathrm{Tr} \left(\boldsymbol{\mu} \cdot \bar{\boldsymbol{\mu}}^{-1} \right) - 3 \right), \tag{27}$$

While similar in appearance to the neo-classical formula of Bladon et al. (1993), there are two notable differences in the presented theory. First, the assumption of non-affine chain motion (described by Eq. (5)) makes the definition of $\boldsymbol{\mu}$ more complex than the typical tensor transformation $\boldsymbol{Q} = \boldsymbol{F}\boldsymbol{Q}_0\boldsymbol{F}^T$ for an affine

mapping of an arbitrary tensor $\boldsymbol{Q}$. Second, the trace of the chain bias tensor $\bar{\boldsymbol{\mu}}$ is constant as the mesogens only influence the orientation of the polymer chains and not their resting length (as discussed previously). While these are noticeable differences, the neo-classical formula will be shown to be a limiting case of the current model in Section 4. Having defined the chain energy density ψ_c, the total free energy density of the system becomes

$$\psi = \frac{G}{2}\left(\mathrm{Tr}\left(\boldsymbol{\mu}\cdot\bar{\boldsymbol{\mu}}^{-1}\right)-3\right) + E\cdot s\left(\lambda^*\right) + K\cdot s\left(J\right), \tag{28}$$

where E and K are penalty multipliers reflecting the high rigidity of the mesogens and incompressibility of the material, respectively, and we defined the penalty function

$$s(x) = x - 1 - \ln x. \tag{29}$$

Note that $s(x)$ is convex for $x > 0$, diverges as $x \to 0$, and is minimized at $x = 1$, making it a suitable penalty function for a scalar quantity x that is assumed to remain unity. Using Eqs. (23) and (24), we arrive at the following definitions for the Cauchy stress $\boldsymbol{\sigma}$ and resultant moment tensor $\boldsymbol{\beta}$:

$$\boldsymbol{\sigma} = G\left[\bar{\boldsymbol{\mu}}^{-1}\cdot(\boldsymbol{\mu}+\boldsymbol{\eta})\right] + K(J-1)\boldsymbol{I}, \tag{30}$$

$$\boldsymbol{\beta} = E(\lambda^*-1)\boldsymbol{g}_{11} + \frac{G}{2\kappa+1}\left[\frac{3\kappa}{\kappa-1}\left(\boldsymbol{\mu}-\mu_{11}\boldsymbol{I}\right)\cdot\boldsymbol{g}_{11} - \boldsymbol{\eta}\right], \tag{31}$$

where $\mu_{11} = \boldsymbol{\mu} : \boldsymbol{g}_{11}$ is the component of $\boldsymbol{\mu}$ in the $\boldsymbol{g}_{11}$ basis. These equations are general in form and may be used to solve the coupled system of governing equations derived in Section 3.1. We note here that the inverse of $\bar{\boldsymbol{\mu}}$ is simple to compute as it is diagonal in the $\boldsymbol{g}_{ij}$ basis (see Eq. (4)). Thus, one can simply invert the coefficients of each term after expanding $\boldsymbol{I} = \boldsymbol{g}_{11} + \boldsymbol{g}_{22} + \boldsymbol{g}_{33}$ to invert the tensor and make use of Eqs. (28) – (31).

3.4. Equilibrium Motion

Before illustrating the basic predictions of the model, let us discuss the physical meaning and advantages of incorporating an independent description of the mesogen motion through the field variable $\boldsymbol{n}$. As discussed previously, it is assumed that the mesogens exist at a more localized lengthscale than that of the bulk material. In this way, the motion of the mesogen is dictated by the forces and torques that are transmitted to it by the polymer network. Let us begin by considering a system in which there are no external body forces or couples. In this case, along with the vanishing of the gradient $\nabla\boldsymbol{n}$, the local balance equations in Eq. (20) are written

$$\begin{aligned} \nabla\cdot\boldsymbol{\sigma} &= \boldsymbol{0}, \\ \boldsymbol{\pi} &= \boldsymbol{0}, \end{aligned} \tag{32}$$

requiring that the resultant moment $\boldsymbol{\pi}$ (and, thus, $\boldsymbol{\beta}$) vanish for all deformations. To explore this concept, let us consider a decomposition of the resultant moment tensor $\boldsymbol{\beta}$ into its scalar components. Due to its definition as the dyadic product $\boldsymbol{\beta} = -\boldsymbol{\pi}\otimes\boldsymbol{n}$, there are only three degrees of freedom – similar to the couple tensor $\boldsymbol{\eta}$. Using a tensor decomposition, we may express them as

$$\begin{aligned} \beta_{11} &= E(\lambda^*-1) + \frac{G}{2\kappa+1}\eta_{11}, \\ \beta_{21} &= \frac{G}{2\kappa+1}\left(\eta_{21} + \frac{3\kappa}{\kappa-1}\mu_{12}\right), \\ \beta_{31} &= \frac{G}{2\kappa+1}\left(\eta_{31} + \frac{3\kappa}{\kappa-1}\mu_{13}\right). \end{aligned} \tag{33}$$

In the system we are considering, each of these components must vanish for a particular realization of the fields $\boldsymbol{x}$ and $\boldsymbol{n}(\boldsymbol{x})$ to be thermodynamically admissible. These equations can then be considered as relating

the stretch λ^* and orientation $\boldsymbol{g}_1$ of the mesogens to that of the polymer matrix undergoing finite deformations. Let us briefly discuss the implicit solutions of each equation when $\boldsymbol{\beta}$ vanishes.

Mesogen Stretch. Even though mesogens are generally considered to be rigid, the theory explicitly considers the relative stiffness E/G of the mesogen and its contribution to locally constraining the motion of polymer chains in a specific direction. We show that increasing this constraint naturally intensifies the network's anisotropy. The tensile equilibrium of the mesogen is described by the vanishing of the first equation in Eq. (33). Thus, we may write

$$\eta_{11} = -\frac{E\,(2\kappa+1)}{G}\,(\lambda^*-1)\,. \tag{34}$$

Using the kinematic definition of $\boldsymbol{\eta}$ in Eq. (11), this may be written in the following quadratic form:

$$(\lambda^*)^2 + \big[\alpha - \boldsymbol{F} : (\boldsymbol{g}_1 \otimes \boldsymbol{n}_0)\,\big]\lambda^* - \alpha = 0, \tag{35}$$

with

$$\alpha = \frac{E\,(2\kappa+1)}{G\chi}. \tag{36}$$

Importantly, we note that as $\alpha \to \infty$ (i.e., the mesogens become much stiffer than the matrix), the solution to the first equation smoothly converges to $\lambda^* = 1$. The ratio α thus defines the relative elasticity of the mesogens with respect to the polymer matrix. While the penalty form of Eq. (29) was chosen to reflect rigid mesogens, the balance of internal forces dictated by Eq. (34) remains valid for smaller values of α. Thus, the present formulation could be used to predict the stretch of nematic elastomers with relatively soft mesogens as well.

Mesogen Rotation. The consideration of an independent mesogen rotation degree of freedom, described by the unit vector $\boldsymbol{g}_1$, enables us to capture the effect of network conformation on the affinity of mesogen rotation. We will demonstrate later that this has important effects on the nonlinear elastic response of the material, including soft and semi-soft elasticity. The shear equilibrium of the mesogen is described by the vanishing of the second and third equations in Eq. (33), such that

$$\eta_{21} = \left(\frac{3\kappa}{1-\kappa}\right)\mu_{12}, \quad \text{and} \quad \eta_{31} = \left(\frac{3\kappa}{1-\kappa}\right)\mu_{13}. \tag{37}$$

Recall that the shear components of $\boldsymbol{\eta}$ reflect the tendency of polymer chains to induce rotations of the mesogen (Fig. 3). Physically, Eqs. (37) enforce a balance between the shear of the polymer network itself and the shear induced onto the mesogens. The degree of network bias, as described by the ratio $3\kappa/(1-\kappa)$ thus becomes highly influential in dictating the rotation of the mesogen. Conceptually, this relates to a higher effective moment arm of a polymer network aligned with the mesogen. Notice that in the limiting case of $\kappa \to 0$, Eq. (37) dictates that the shear components of $\boldsymbol{\eta}$ must vanish. This will be discussed further in Section 4.

4. Limiting cases

Let us begin exploring the predictions of our model by first contextualizing its form to previously developed models. The statistical theory developed here is convenient in terms of its physical interpretation. Using this as a foundation, incorporating new physics such as non-linear chain behavior (Lamont et al., 2021) or dynamic bonding (Vernerey, 2022) may be done in a physically-relevant setting. With this said, the form of the free energy presented in Eq. (28) is not as transparent as a hyperelasticity formulation, for instance. For better transparency, let us explicitly write ψ in terms of $\boldsymbol{F}$ and $\boldsymbol{n}$ using the definition of $\boldsymbol{\mu}$ in Eq. (10):

$$\begin{aligned}\psi(\boldsymbol{F},\boldsymbol{n}) = \frac{G}{2}\mathrm{Tr}\Big[\boldsymbol{F}\cdot(\boldsymbol{\mu}_0+\chi\boldsymbol{\rho}_0)\cdot\boldsymbol{F}^T\cdot\bar{\boldsymbol{\mu}}^{-1} + \chi\left(\boldsymbol{n}\otimes\boldsymbol{n} - \boldsymbol{F}\cdot(\boldsymbol{n}_0\otimes\boldsymbol{n}) - (\boldsymbol{n}\otimes\boldsymbol{n}_0)\cdot\boldsymbol{F}^T\right)\cdot\bar{\boldsymbol{\mu}}^{-1} - \boldsymbol{I}\Big] \\ + E\,(||\boldsymbol{n}|| - 1 - \ln||\boldsymbol{n}||) + K\,(J-1-\ln J)\,.\end{aligned} \tag{38}$$

Within the trace operation, we clearly observe two terms separated by the coefficient χ. In this section, we illustrate two limiting cases of our model, which occur for specific values of χ and κ. In both cases, this theory converges identically to previously established mechanical theories.

4.1. Convergence to the neo-classical theory for affine chain motion ($\chi \to 0$)

The most prominent theory for nematic liquid crystal elastomers has been presented by Bladon, Terentjev, and Warner in Bladon et al. (1993). In their so-called 'neo-classical' theory of polymer elasticity, they also proposed a transversely isotropic chain distribution about some principal director for a nematic elastomer. In their case, the end-to-end vector $\boldsymbol{r}$ of each polymer chain was assumed to deform affinely with the macroscopic deformation $\boldsymbol{F}$ (i.e., Eq. (5) becomes $\boldsymbol{r} = \boldsymbol{F} \cdot \boldsymbol{r}_0$). The free energy density of the neo-classical theory is then typically written in the form

$$\psi_c = \frac{G}{2} \mathrm{Tr} \left(\boldsymbol{l}_0 \cdot \boldsymbol{F}^T \cdot \boldsymbol{l}^{-1} \cdot \boldsymbol{F} \right), \tag{39}$$

where $\boldsymbol{l}$ is the effective step-length tensor with initial value $\boldsymbol{l}_0$. Notice that an equivalent form is recovered by our model in the limiting case of $\chi \to 0$. Physically, this corresponds to the polymer network existing at a much larger lengthscale than the mesogens ($r_0 \gg \ell_0$), making their contributions to the motion of the polymer network negligible. Alternatively, in the context of the generalized continuum, this equates to the vanishing of microinertia (and, thus, convergence to a standard continuum description). To further compare these two approaches, let us consider the form of $\boldsymbol{l}$ presented by Bladon et al. (1993) in its principal frame. Referring to the definitions in Eq. (2) of the effective step-lengths $r_\parallel$ and $r_\perp$, it is expressed as

$$\boldsymbol{l} = r_\parallel \left(\boldsymbol{g}_1 \otimes \boldsymbol{g}_1 \right) + r_\perp \left(\boldsymbol{g}_2 \otimes \boldsymbol{g}_2 + \boldsymbol{g}_3 \otimes \boldsymbol{g}_3 \right). \tag{40}$$

In the neo-classical theory, the inversion of the step-length tensor $\boldsymbol{l}$ appearing in Eq. (39) reduces the parameterization of the free energy to one non-dimensional parameter $r = r_\parallel / r_\perp$. This is commonly referred to as the step-length ratio. It is sometimes convenient to instead express the free energy in terms of the normalized step-length tensor $\hat{\boldsymbol{l}} = \boldsymbol{l}/r_\perp$, which is written

$$\hat{\boldsymbol{l}} = (r-1)\, \boldsymbol{g}_1 \otimes \boldsymbol{g}_1 + \boldsymbol{I}. \tag{41}$$

In this theory, the degree of nematic order, Q (which ranges from $-1/2$ to 1, where $Q = 1$ indicates a fully aligned state), is incorporated into their description of elasticity via the tensor $\bar{\boldsymbol{l}}$ and parameterized by r. For this reason, the step-length ratio r becomes an important parameter in describing the response of nematic liquid crystal elastomers (Warner and Terentjev, 2007). We therefore finally note the relationship between the step-length ratio r and the chain bias parameter κ presented in this theory as:

$$r = \frac{\kappa - 1}{2\kappa + 1}. \tag{42}$$

While this definition only applies directly in the limiting case of $\chi \to 0$, its usage will be useful when presenting the predictions of the full formulation. Finally, we note that in this limiting case, the resultant moment $\boldsymbol{\pi}$ identically vanishes for all $\boldsymbol{n}$. The motion of the director is, thus, solved for by energy minimization as in the neo-classical theory.

4.2. Convergence to the anisotropic neo-Hookean model for isotropic polymer chains ($\kappa \to 0$)

The second limiting case of our model occurs when there is no bias of the mesogens imposed on the polymer network. In this case, the polymer network is isotropic about $\boldsymbol{g}_1$ and remains uninfluenced by the mesogens during deformation. This equates to defining $\kappa = 0$ and thus

$$\boldsymbol{\mu}_0 = \bar{\boldsymbol{\mu}}^{-1} = \boldsymbol{I}. \tag{43}$$

Let us first discuss the solution to the balance of internal stress. In the case of extremely rigid mesogens, we may take $\lambda^* = 1$ as defined previously. From the remaining balance equations, we use Eq. (10) and Eq. (37) to yield the following necessary conditions:

$$\begin{aligned} \boldsymbol{g}_2 \cdot (\boldsymbol{F} \cdot \boldsymbol{n}_0) = 0, \\ \boldsymbol{g}_3 \cdot (\boldsymbol{F} \cdot \boldsymbol{n}_0) = 0. \end{aligned} \tag{44}$$

These equations provide implicit solutions for the nematic orientation $\boldsymbol{g}_1$ (as a unit vector is only parameterized by two angles in three-dimensional space). From the definition of the dot product, this system requires the vector $\boldsymbol{F} \cdot \boldsymbol{n}_0$ to be orthogonal to both $\boldsymbol{g}_2$ and $\boldsymbol{g}_3$ and, therefore, be parallel to $\boldsymbol{g}_1$. In the condition that $\lambda^* = 1$ and $\boldsymbol{n} = \boldsymbol{g}_1$ is a unit vector, we immediately arrive at the surprisingly simple solution for $\boldsymbol{n}$:

$$\boldsymbol{n} = \frac{\boldsymbol{F} \cdot \boldsymbol{n}_0}{||\boldsymbol{F} \cdot \boldsymbol{n}_0||}, \tag{45}$$

where $||\cdot||$ denotes the euclidean norm of a quantity. In other words, when the polymer network is isotropic and unbiased by the nematic director, our theory predicts an affine, but length-preserving, rotation of $\boldsymbol{n}_0$ with the applied macroscopic deformation $\boldsymbol{F}$. The implications of this are immediately observed by inserting this solution into the kinematic equations and evaluating the resulting free energy and stress. Following a straightforward derivation in Appendix 8.4, we arrive at the following definition for the chain energy ψ_c:

$$\psi_c = \frac{G}{2}\left[(I_1 - 3) + \chi\left(\sqrt{I_4} - 1\right)^2\right], \tag{46}$$

where I_1 and I_4 are the first and fourth tensor invariants of the right Cauchy-Green tensor $\boldsymbol{C} = \boldsymbol{F} \cdot \boldsymbol{F}^T$. Note that the latter of which is written $I_4 = \boldsymbol{n}_0 \cdot (\boldsymbol{F}^T \cdot \boldsymbol{F}) \cdot \boldsymbol{n}_0$. In other words, in this limiting case, our model converges to an anisotropic hyperelasticity formulation. Moreover, this particular form of ψ_c aligns exactly with the fiber-reinforced neo-Hookean rubber proposed nearly forty years ago by Spencer (1985). This was also observed by a previous model proposed by our group in Lalitha Sridhar and Vernerey (2020), which assumed affine deformation of the mesogen *a priori*. As a final note, it is clear that when χ goes to 0 in this model, we arrive at a nearly incompressible neo-Hookean formulation.

5. Uniaxial tension of an aligned nematic

We now illustrate the basic predictions of our model using a constant set of boundary conditions. It is common practice to deform nematic elastomers along an offset angle to their director to induce a new alignment of chains or probe its anisotropic mechanical characteristics. Let us consider such a test, in which, we apply a stretch F_{11} in the $\boldsymbol{e}_1$ direction. Meanwhile, the initial director $\boldsymbol{n}_0$ is oriented at an angle θ_0^* with $\boldsymbol{e}_1$. To simplify the problem, we assume that there are no out-of-plane perturbations and the rotation of the nematic director is restricted to the $\boldsymbol{e}_1 \times \boldsymbol{e}_2$ plane. Assuming our material to be incompressible, the deformation gradient $\boldsymbol{F}$ takes the following form:

$$\boldsymbol{F} = F_{11}\boldsymbol{e}_1 \otimes \boldsymbol{e}_1 + F_{12}\boldsymbol{e}_1 \otimes \boldsymbol{e}_2 + F_{22}\boldsymbol{e}_2 \otimes \boldsymbol{e}_2 + \frac{J}{F_{11}F_{22}}\boldsymbol{e}_3 \otimes \boldsymbol{e}_3, \tag{47}$$

where the shear term F_{12} is known to accompany rotations in the director for a nematic elastomer. Note that in the nearly incompressible formulation, the solution $J \approx 1$ is expected for a correctly calibrated penalty K and its appearance in Eq. (47) is a formality. The elastic energy $\psi(\boldsymbol{F}, \boldsymbol{n})$ is thus a function of three kinematic quantities and the field variable $\boldsymbol{n}$. With this said, for each combination of F_{11}, F_{22} and F_{12}, the nematic director field $\boldsymbol{n}$ must be solved to satisfy the internal balance of linear momentum. In this section, we are therefore considering the solution to the following set of nonlinear equations:

$$\sigma_{22} = \sigma_{33} = \sigma_{12} = 0, \tag{48}$$

$$\boldsymbol{\beta} = \boldsymbol{0}. \tag{49}$$

Generally, the solution to these equations is not trivial due to the coupling between the deformation gradient $\boldsymbol{F}$ and the director field $\boldsymbol{n}$. Thus, it should be solved numerically for each value of F_{11}. In the following sections, we illustrate the basic predictions of our model using these boundary conditions computed at a stress point.

5.1. Characteristic behavior at nearly orthogonal loading

Let us begin by considering the characteristic behavior of this model as parameterized by the chain bias κ and the rotational microinertia χ. Due to the coupled behavior of the nematic director with the deformation field, the constitutive behavior is not simple to illustrate analytically. Instead, we consider three quantities that together reflect the behavior of the material. They are the normalized Cauchy stress response σ_{11}/G, the current director orientation θ^*, and the out-of-plane contraction $F_{33} = 1/(F_{11}F_{22})$. Due to their convenient analytical forms, the limiting cases presented in Section 4 will be used for comparison whenever possible. To best illustrate the model, we first consider the case of applying uniaxial loading nearly orthogonal to the initial nematic director ($\theta_0^* = 89°$ is used to avoid numerical complications associated with bifurcation instabilities).

In Figure 5, we plot the behavior of a nematic elastomer with mild chain bias ($\kappa = 0.5$) for varying values of the rotational microinertia χ. Let us first briefly discuss the well-known neo-classical response illustrated by the dashed curve labeled $\chi \to 0$. This curve is the 'ideal' soft elastic response first presented in Bladon et al. (1993) and heavily studied in subsequent literature. In brief, there is no change in energy, and thus a stiffness of zero, up until the critical stretch $\lambda_c = \sqrt{r}$. During this time, the director rotates fully from its initial orientation to become exactly in line with the applied deformation. Meanwhile, the lateral contraction of the specimen is entirely in-plane (indicated by $1/(F_{11}F_{22})$ remaining unity). After the critical stretch, the director remains in line with the loading direction, and the response resembles that of a reinforced elastomer. Increasing χ results in divergence from 'ideal' soft elasticity and begins to resemble a 'semi-soft' response. In particular, we may note the alternative limiting case of $\kappa \to 0$, which reflects the behavior of a fiber-reinforced neo-Hookean rubber (Spencer, 1985). By increasing χ, the effect of the stiff mesogens begins to dominate the response, and the behavior converges to the dashed black curve. At small strains, we notice that the intermediate values of χ follow the dashed black line for a short time before approaching the neo-classical predictions. In this way, we may consider $\kappa \to 0$ and $\chi \to 0$ as two extremes that generally bound our response (note that this is not an exact identity).

To further explore this observation, let us instead observe the changes that occur when varying κ. In Figure 6, we plot the behavior of a nematic elastomer with $\chi = 0.5$ for varying values of chain bias. Generally, we observe a very similar (albeit, inverted) trend as before. This time, by decreasing κ, we observe a gradual convergence to the fiber-reinforced neo-Hookean rubber. As in the previous case, the small-strain behavior generally follows this curve, which eventually diverges and begins to resemble neo-classical behavior. This point of divergence is always accompanied by a sudden increase in the rate of mesogen rotation θ^* with respect to the applied stretch as well as anisotropic transverse contractions. We may, therefore, consider both κ and χ as affecting the degree of non-affine motion of the mesogens.

To summarize the characteristic behavior presented in Figs. 5 and 6, we may refer to three regimes of response during an applied stretch. At small strains, director rotation is minimal and the lateral contractions are isotropic. The response, therefore, closely follows the predictions of the fiber-reinforced neo-Hookean rubber. The second regime is marked by an increase in the rate of director rotation. Formally, this may be thought of as the knee-point or point of maximum curvature on the θ^* vs. F_{11} curve. In this regime, motion is highly non-affine, and we predict a unique semi-soft behavior that has not been predicted by other theories. Finally, after the director rotation has completed ($\theta^* \to 0$), motion is once again affine. Our theory predicts a hybrid formulation that is primarily bound between the fiber-reinforced neo-Hookean theory and the neo-classical theory. In the following sections, we study these regimes in-depth to provide a full overview of the model's predictions.

5.2. Small strain anisotropy

As discussed previously, the existence of a stiff phase at a given orientation θ_0 from some applied deformation induces high degrees of anisotropy in the material. To investigate this anisotropy, many researchers

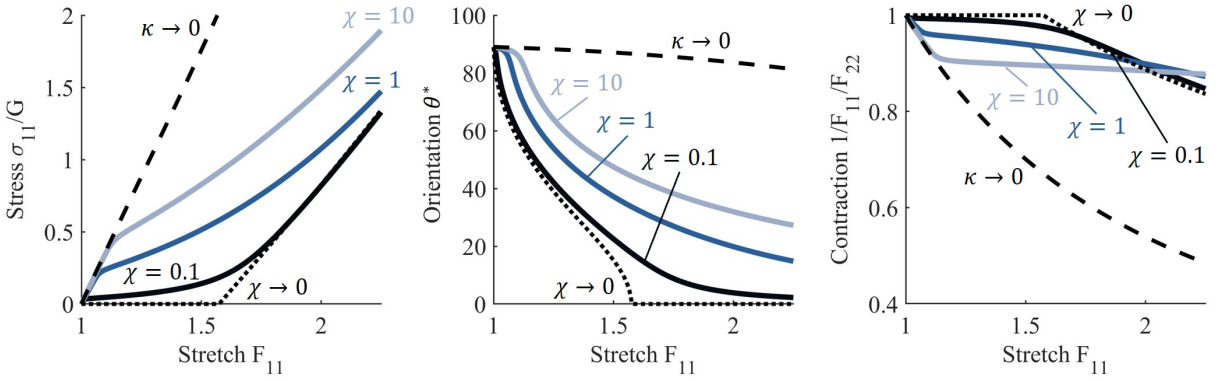

Figure 5: Stress, orientation, and contraction for varying χ during uniaxial tension orthogonal to $\boldsymbol{n}_0$ for a nematic elastomer with $\kappa = 0.5$. The dashed curves reflect the limiting cases discussed in Section 4. For clarity, the black dashed curve representing $\kappa \to 0$ is only illustrated for the case of $\chi = 10$.

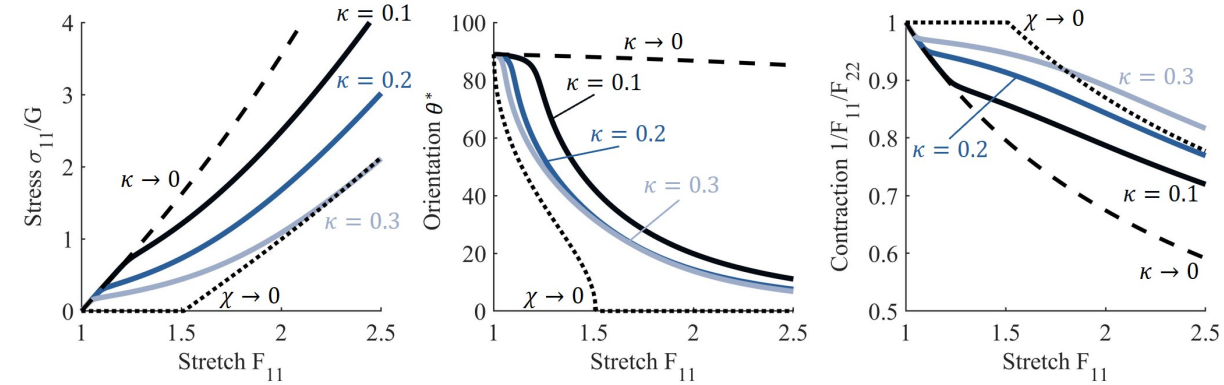

Figure 6: Stress, orientation, and contraction for varying κ during uniaxial tension orthogonal to $\boldsymbol{n}_0$ for a nematic elastomer with $\chi = 0.5$. The dashed curves reflect the limiting cases discussed in Section 4. For clarity, the black dashed curve representing $\chi \to 0$ is only illustrated for the case of $\kappa = 0.3$.

apply a deformation at various angles to the nematic director and measure the linear stiffness, E_0 of the response. Here, we may formally define this measure under the current boundary conditions as

$$E_0 = \lim_{F_{11} \to 1} \frac{\partial \sigma_{11}}{\partial F_{11}}. \tag{50}$$

Figure 7a-b displays the normalized linear modulus E_0/G versus the loading angle θ_0 for varying χ and κ. Generally, increasing χ tends to increase the initial stiffness of the material, which is expected for rigid mesogens. In contrast, increasing the chain bias κ tends to decrease the initial stiffness. The initial modulus of an anisotropic material may, thus, be used to determine the degree of bias κ of its chains as well as the relative lengthscale as parameterized by χ in our model. We particularly note the work of Mistry and Gleeson (2019), in which a monodomain liquid crystal elastomer sample was stretched in uniaxial tension at a variety of loading angles. By observing the initial slope of the stress-strain curve, they calculated the linear modulus as a function of loading angle θ_0, whose curve greatly resembles the trend illustrated in Fig. 7a. Notably, this system did not display soft elasticity at large initial director angles – indicating a small degree of chain bias. The motion of the director measured by this group also closely followed the affine prediction recovered in the case of $\kappa \to 0$.

In many practical applications, it is desirable to maximize the difference between the linear modulus $E_0^{\parallel}$ in the direction of $\boldsymbol{n}_0$ and the linear modulus $E_0^{\perp}$ in the direction perpendicular to $\boldsymbol{n}_0$. This is of particular

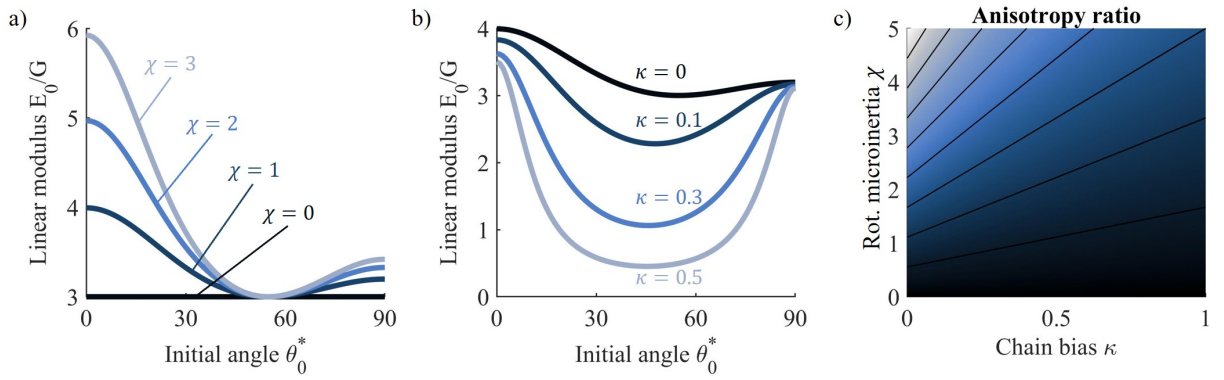

Figure 7: Summary of model predictions for the linear modulus E_0 with varying model parameters. a) Normalized linear modulus E_0/G versus initial director angle θ_0^* for varying rotational microinertia χ with $\kappa = 0$. b) Normalized linear modulus E_0/G versus initial director angle θ_0^* for varying chain bias κ with $\chi = 1$. c) Contour view of the anisotropy ratio E_{ratio} defined in Eq. (52). Solid black lines are iso-contours at intervals of 0.25.

interest to the creation of efficient dielectrics (Davidson et al., 2019) and electrically-controlled structural materials (Guin et al., 2018). For this reason, the anisotropy ratio

$$E_{ratio} = E_0^{\parallel}/E_0^{\perp} \tag{51}$$

is often cited. Due to the out-of-plane behavior of the nematic system, the initial stiffness has a unique dependency on the initial angle of the director. Using some small-strain assumptions, we may analytically solve for the anisotropy ratio E_{ratio} in uniaxial conditions with our model. We first linearize the constitutive stress behavior in Eq. (30), followed by using small-angle assumptions to simplify the micro-balance of linear momentum in Eq. (33). After some simple algebra, we arrive at the analytical form:

$$E_{ratio} = \frac{\chi + 4(2\kappa + 1)}{4(2\kappa + 1)}. \tag{52}$$

The surface defined by E_{ratio} is plotted in Fig. 7c for $0 \leq \chi \leq 10$ and $0 \leq \kappa \leq 1$. According to the predictions of our model, the anisotropy ratio is maximized for low values of chain bias ($\kappa \approx 0$) and networks with larger mesogens. These conditions result in a network with affinely rotating mesogens that provide significant stiffness when loaded in the parallel direction. Interestingly, as the rotational microinertia χ approaches 0, the anisotropy ratio approaches 1 for all values of chain bias. This is due to the 'ideal' soft elasticity predicted by the neo-classical model. These predictions may assist in the informed design of materials with larger anisotropy ratios with various applications in fields such as soft robotics (Annapooranan et al., 2023; Xu et al., 2024) and bioengineering (Shaha et al., 2020).

5.3. Finite deformation anisotropy

Let us now more completely characterize the anisotropy predicted by our model by considering finite deformations. This may be illustrated by observing the model's predictions when loading the nematic elastomer at an arbitrary angle θ_0^* to the initial director. In Fig. 8a, we again plot the normalized stress σ_{11}, director orientation θ^*, and lateral contraction $F_{33} = 1/(F_{11}F_{22})$ when loading the elastomer at three different initial angles of $\theta_0^* = 30$, $\theta_0^* = 45$, and $\theta_0^* = 60$. For this system, we have used a chain bias of $\kappa = 0.5$ and a relative moment of inertia $\chi = 1$. In general, we predict a stiffer response when loading more parallel to the director (i.e., lower θ_0^*), as would be expected. The stress response at large strains (as $\theta^* \to 0$) is characterized by convergence to a constant rate of stiffening with increasing F_{11}. This is illustrated by the inset in Fig. 8a, in which, it can be observed that the slope $\partial\sigma_{11}/\partial F_{11}$ approaches a linear trend at large stretches. Interestingly, even though the initial value of θ^* is different for each curve, the convergence of

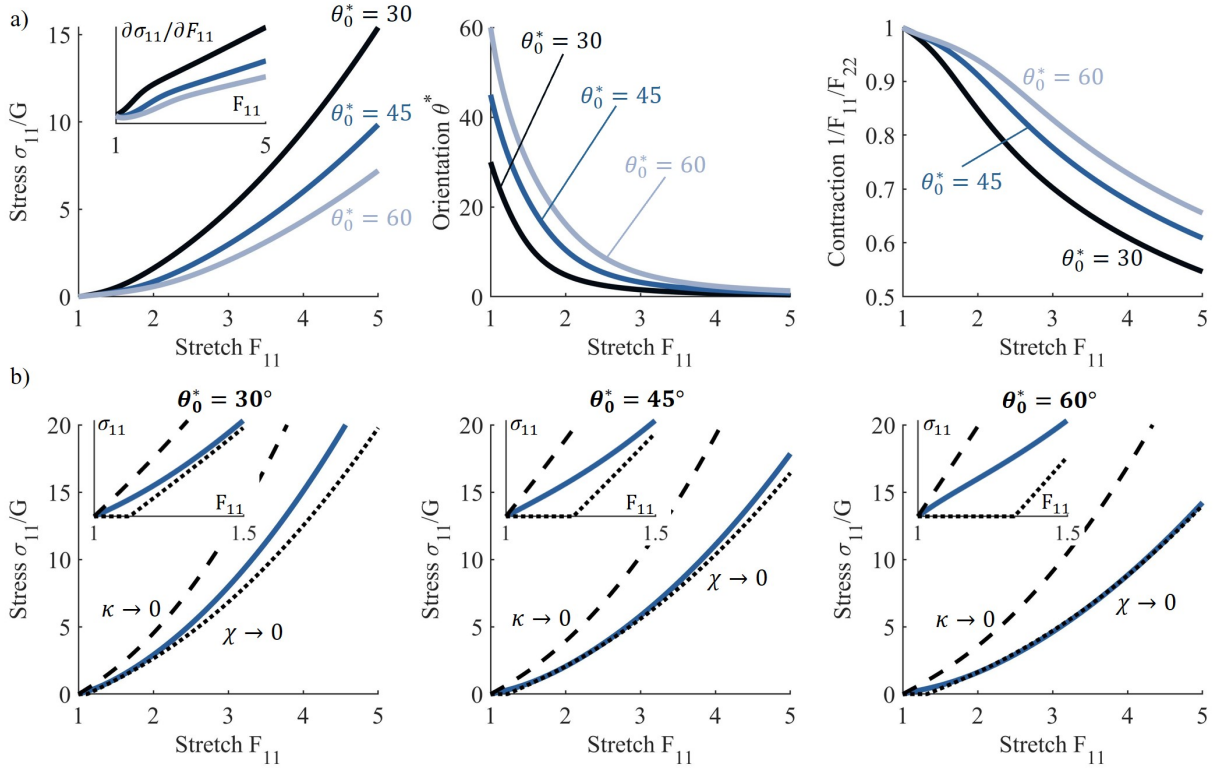

Figure 8: a) Stress, orientation, and lateral contraction in uniaxial tension when loading at $\theta_0^* = 30$, $\theta_0^* = 45$, and $\theta_0^* = 60$ for a nematic elastomer with chain bias $\kappa = 0.5$ and rotational microinertia $\chi = 1$. The inset illustrates the slope $\partial\sigma_{11}/\partial F_{11}$ for the respective curves. b) Stress response for a nematic elastomer with chain bias $\kappa = 0.5$ and rotational microinertia $\chi = 1$ with limiting cases illustrated.

$\theta^* \to 0$ is approached at a similar value of stretch. This implies a roughly exponential trend or realignment with this set of parameters. We also note that the lateral contraction becomes more isotropic at lower initial angles but favors in-plane contraction at higher initial angles. This reflects the in-plane softening that occurs during director reorientation.

In general, the finite deformation response is still roughly bounded by the two model limits as defined in Section 5.1. In Fig. 8b, we plot only the stress response for the same nematic elastomer when loaded with $\theta_0^* = 30$, $\theta_0^* = 45$, and $\theta_0^* = 60$. This time, we also illustrate the predictions of the fiber-reinforced eo-Hookean model ($\kappa \to 0$) and the neo-classical model ($\chi \to 0$). At very small strains, as observed previously, the stiffness of our model is closer to that of the $\kappa \to 0$ case. At all initial angles, the response then softens due to the non-affine director reorientation and appears to approach the predictions of the neo-classical model. At much larger deformations, however, the rate of stiffening becomes bound between these two limiting cases. This is most clearly observed in the case of $\theta_0^* = 30$, where the large-strain behavior predicted by our model falls between the two dashed lines. Note that this is generally the case, and will occur for the cases of $\theta_0^* = 45$ and $\theta_0^* = 60$ at a larger stretch.

5.4. Bifurcation instability at exactly orthogonal deformations

As observed in Section 5.1, when loaded nearly orthogonal to the initial nematic director, the second phase of the response is marked by a sudden divergence from the predictions of the fiber-reinforced neo-Hookean model. Let us now consider the predicted behavior when loaded exactly orthogonal to the director ($\theta_0^* = 90°$). In general, we expect that the director remains orthogonal up to a critical stretch F_{11}^{crit}. At this stretch, there is a sudden rotation of the director either clockwise or counter-clockwise with no energetic

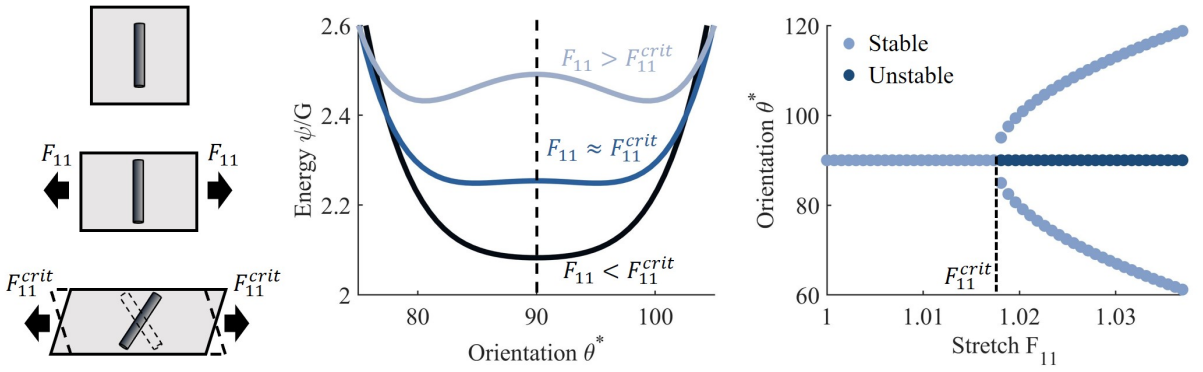

Figure 9: Illustration of the bifurcation problem studied here. (left) energy curves at a constant stretch for varying director orientation θ^*. Curves are illustrated just before bifurcation, during bifurcation, and just after bifurcation. (right) Equilibrium solutions of θ^* illustrating the pitchfork bifurcation. Points are designated as 'stable' or 'unstable' according to their convexity.

preference. This may be formally classified as a bifurcation instability and is marked by a change in the convexity of the free energy ψ at a stretch F_{11}^{crit}. To better characterize this phenomenon, we may perform a basic instability analysis (Santisi d'Avila et al., 2016; Pampolini and Triantafyllidis, 2018). As the variational problem is ill-defined over Ω, we may consider instead the bifurcation at an isolated stress point for the case of $\boldsymbol{\xi} = \mathbf{0}$. We define $\boldsymbol{\varrho} \equiv \{\boldsymbol{F}, \boldsymbol{n}\}$ to be the subset of kinematic descriptors for the body Ω that does not include the gradient $\boldsymbol{\xi}$. At a single stress point, the equilibrium solution $\boldsymbol{\varrho}_{eq}$ is defined as satisfying the vanishing of the first variation of the potential energy:

$$\frac{\partial \psi}{\partial \boldsymbol{\varrho}} \cdot \delta \boldsymbol{\varrho} = 0. \tag{53}$$

At small deformations, the director remains orthogonal to the loading direction as it remains in a stable equilibrium. In this regime, the transverse contractions are isotropic ($F_{22} = F_{33}$) and no shearing is observed. We may, thus, define the principal solution $\overset{0}{\boldsymbol{\varrho}}_{eq} \subset \boldsymbol{\varrho}_{eq}$ as the equilibrium solution at small strains before the instability. More explicitly, we write

$$\overset{0}{\boldsymbol{\varrho}}_{eq} = \begin{cases} \overset{0}{\boldsymbol{F}} = F_{11}\boldsymbol{e}_1 \otimes \boldsymbol{e}_1 + 1/\sqrt{F_{11}}\,(\boldsymbol{e}_2 \otimes \boldsymbol{e}_2 + \boldsymbol{e}_3 \otimes \boldsymbol{e}_3)\,, \\ \overset{0}{\boldsymbol{n}} = \boldsymbol{n}_0. \end{cases} \tag{54}$$

For all deformations, $\overset{0}{\boldsymbol{\varrho}}_{eq}$ is an equilibrium solution as it satisfies the variational requirement in Eq. (53). The bifurcation occurs at the stretch F_{11}^{crit} at which the convexity upon the principal solution changes. To avoid further lengthy derivations, we here calculate a numerical solution to the bifurcation problem. To do this, we first calculate the full energy surface of $\psi(\boldsymbol{\varrho})$ for an applied stretch F_{11}. As for all problems studied in this section, a particular solution $\bar{\boldsymbol{\varrho}}$ is constrained by the traction-free condition as well as the balance of internal linear momentum as defined in Eqs. (48) – (49). We may, thus, define the elastic energy $\bar{\psi} \equiv \psi(\bar{\boldsymbol{\varrho}})$ of the particular solution $\bar{\boldsymbol{\varrho}}$ and only consider a variation $\delta\theta^*$ in the director orientation along this solution. We then search for the stretch F_{11}^{crit} at which the convexity $\partial^2\bar{\psi}/\partial\theta^{*2}$ becomes zero (indicating a change in sign). In Fig. 9, we plot the normalized energy ψ/G versus the director orientation θ^* for an applied stretch just before, just after, and approximately at the critical stretch F_{11}^{crit} for a reference set of parameters ($\chi = 0.1$ and $\kappa = 0.1$). The bifurcation is observed as the extrema located at $\theta^* = 90°$ transforms from a minimum to a maximum. After reaching the critical stretch, two symmetric minima appear for clockwise and counter-clockwise rotations of the mesogen. To better illustrate the pitchfork bifurcation, we may also plot the equilibrium solutions $\theta^* \in \boldsymbol{\varrho}_{eq}$ versus the applied stretch F_{11} and classify them as stable or unstable based on their convexity (Fig. 9).

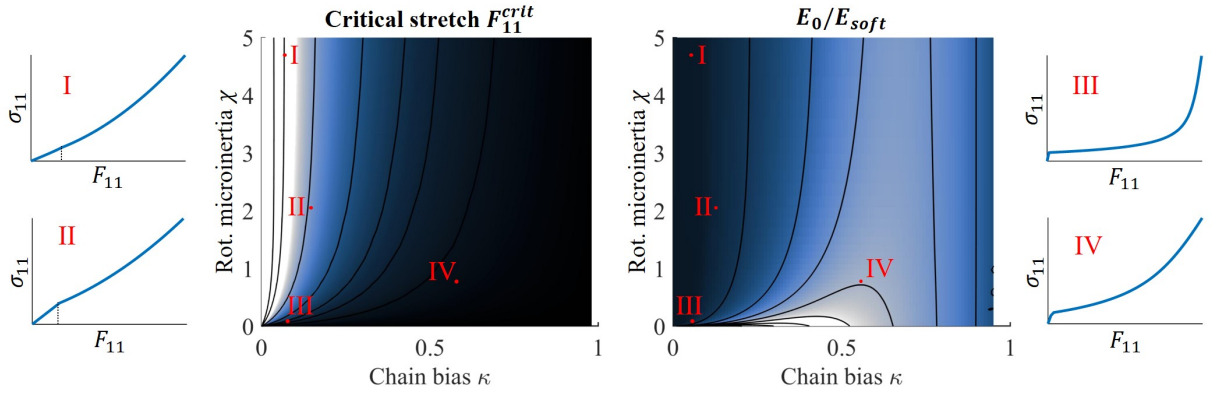

Figure 10: Parameter sweep of the instability behavior of the nematic elastomer. All values are normalized between 0 and 1 for convenience, where darker colors indicate values close to 0 and lighter colors indicate values close to 1. Solid lines are iso-contours for easier visualization. The points I-IV were chosen to illustrate characteristic behaviors as illustrated by their stress-stretch response.

The analysis described above can be performed for the full parametric range of κ and χ. In general, we are interested in how F_{11}^{crit} changes, as this marks the onset of semi-soft elasticity, as well as the degree of softening observed by the system. We, therefore, plot surfaces of the critical stretch F_{11}^{crit} and softening ratio E_0/E_{soft} for $0 \leq \kappa \leq 1$ and $0 \leq \chi \leq 5$ in Fig. 10. The soft modulus E_{soft} is the slope of the σ_{11} vs. F_{11} immediately after the bifurcation. In these contours, all data are normalized between 0 and 1 for simpler comparison, where darker colors indicate values close to 0 and lighter colors indicate values close to 1. We also plot the normalized stress response at various portions of the surface (labeled I-IV in Fig. 10) to highlight the characteristic behaviors that our model predicts.

On the surface of the critical stretch F_{11}^{crit}, the behavior as $\kappa \to 0$ is divergent (i.e., $F_{11}^{crit} \to \infty$). This is reflective of the stability of the fiber-reinforced neo-Hookean model, which remains stable for all deformations. In other words, we always predict a bifurcation for some $F_{11}^{crit} \geq 1$ for any $\kappa \neq 0$. In the other extreme, as $\chi \to 0$, we predict immediate bifurcation is subsequent director realignment as in the neo-classical model. In contrast, as χ is increased past $\chi \approx 1$, the system becomes less sensitive to further increases in χ. Note that for most values of κ, the critical stretch occurs at relatively small deformations. The corresponding surface of critical stress σ_{11}^{crit} is, thus, qualitatively very similar to the critical stretch surface as at small strains there is a linear correlation between stress and strain.

The semi-soft behavior predicted by our model is better understood when looking at both the critical stretch F_{11}^{crit} and the softening ratio E_0/E_{soft} together. Interestingly, the surface of E_0/E_{soft} is not qualitatively similar to that of F_{11}^{crit}. We may first note that as $\chi \to 0$, we also observe divergent behavior with $E_0/E_{soft} \to 0$ as we approach the 'perfect' soft elastic response of $E_{soft} = 0$. As for the trend with κ, it appears that we predict that for the highest softening ratio, the middle values of $\kappa \approx 0.5$ are preferred. In general, low values of χ and κ predict the most 'typical' semi-soft behavior as illustrated by curves III and IV in Fig. 10.

5.5. Experimental validation: soft, semisoft, or hyperelastic?

Let us now consider a more relevant depiction of the uniaxial tension response by comparing the model's predictions to experimental data on monodomain nematic liquid crystal elastomers. There is a large pool of experimental literature on nematic liquid crystal elastomers that has been historically difficult to unify. Some systems display a nearly ideal soft elastic response, while some simply resemble a highly extensible rubbery material. In between these two extremes, perhaps a majority of nematic elastomers display the so-called "semi-soft" behavior, in which, there is an initial stiffness that eventually yields and softens, followed by a subsequent stiffening at larger strains. The semi-soft behavior has been previously attributed to network imperfections (see Verwey and Warner (1997) and subsequent publications), which successfully

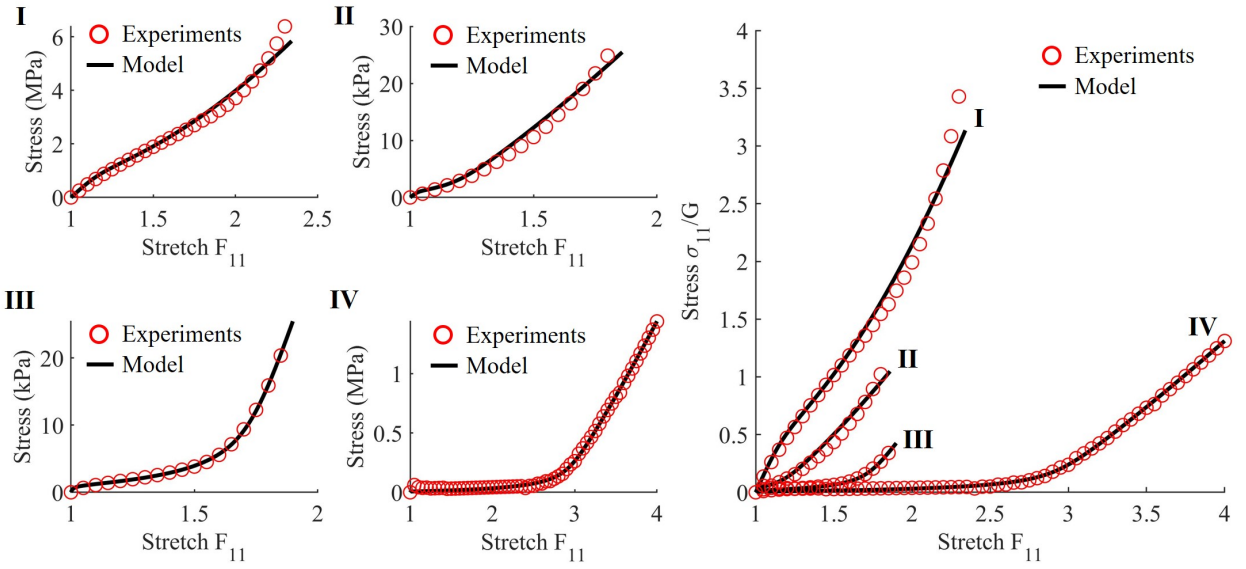

Figure 11: Model fitting for four different monodomain nematic LCEs pulled orthogonal to the nematic director. During fitting, the initial director angle was allowed to vary between $85° \leq \theta_0^* \leq 90°$. Left curves (I-IV) present the true stress versus true strain data for the references cited in Table 1. On the right-most plot, all curves were normalized by their shear modulus G for better visibility.

predicted some of the features of semi-soft elasticity observed in nematic elastomers. As described in the previous section, our model predicts a different type of semi-soft response due to the non-affine network assumption. We assert here that the characteristic behavior predicted by our model reflects many of the responses observed in experimental systems.

Figure 11 illustrates the uniaxial response of four different nematic LCEs pulled roughly orthogonal to the initial director ($\theta_0^* \approx \pi/2$). Each response is quite different in terms of (i) initial stiffness, (ii) softening behavior, and (iii) large-strain response. In Table 1, we provide the fitted model parameters and citation for each curve. It is worth noting that the initial director angle θ_0^* was allowed to vary between 85° and 90° during the fitting procedure to allow some leniency in the initial conditions. The first thing to note is that the fitted values for the rotational microinertia χ appear to be quite small – with all of them being less than one. This would perhaps imply that a more natural parameter for these systems is the simple ratio of lengths $\gamma\ell_0/r_0$, which ranges from $\gamma\ell_0/r_0 \approx 0.2$ to $\gamma\ell_0/r_0 \approx 0.9$ for the systems we fit in this section. As expected, the system with the largest chain bias from the work of He et al. (2020) observes the longest semi-soft plateau due to its well-known scaling with $\sqrt{r}$ (see Eq. (42) and discussion in Bladon et al. (1993) and Warner and Terentjev (2007)).

Perhaps the most drastic difference between the soft elasticity that we predict and that predicted by other theories (such as the classical formulation of Verwey and Warner (1997)) is the relatively continuous transition from the semi-soft plateau into the large deformations regime. Indeed, the exact point of departure from the semi-soft plateau in curves III and IV in Fig. 11 is not immediately apparent. Generally, this is due to the gradual trend of director reorientation predicted by our model. We also note that the large deformation response of the systems in curves I and II is not well captured by this formulation. In general, it appears that these materials stiffened much more at larger strains, which is likely due to nonlinear behavior in the polymer network. Our fitting could, thus, likely be improved by using a nonlinear energy functional for the polymer network, such as one reflecting Langevin statistics (Lamont et al., 2021).

Table 1: Fitted model parameters for monodomain nematic LCEs

Curve number	Reference	Shear modulus G	Rot. microinertia χ	Chain bias κ
I	Mistry and Gleeson (2019)	1.8 MPa	0.80	0.14
II	Clarke et al. (2001)	12 kPa	0.04	0.08
III	Clarke et al. (2001)	60 kPa	0.06	0.37
IV	He et al. (2020)	1.1 MPa	0.10	0.70

6. Conclusion

In this study, we presented a micro-mechanically formulated theory for nematic elastomers undergoing finite deformations. The key feature of this model is its foundations in statistical network geometry and physically motivated parameters. By decoupling the motion of the polymer chains with that of the nematic director, our theory naturally predicts non-affine mesogen rotations by enforcing classical continuum thermodynamics laws such as the balance of linear momentum. Notably, our model converges identically to previously established mechanical theories at the extreme ends of the parametric space. In particular, the well-established neo-classical theory of Bladon et al. (1993) is realized when the lengthscale of the polymer network is much greater than the lengthscale of the mesogens. Using this formulation, we illustrated the unique semi-soft behavior predicted by our model in terms of its (i) small-strain anisotropy, (ii) finite deformation anisotropy, and (iii) bifurcation instability. Finally, we validated our model using experimental data on four different monodomain nematic liquid crystal elastomers.

While modern theories on nematic elastomers exist (such as the nonlinear viscoelasticity theory of Wang et al. (2022)), the current formulation is particularly promising in its flexibility due to the foundational description of the system at the level of a chain-mesogen unit. This is expressed by our separate descriptions of the polymer network and the liquid-crystalline mesogens. In this way, more complex and realistic physics may be incorporated at the level of the polymer chains or the mesogens directly. In particular, we may consider polymer chains crosslinked by 'dynamic' junctions (Vernerey, 2022), which have become increasingly popular in the field of liquid crystal elastomers (Saed et al., 2021). The large-strain behavior may also be better captured by incorporating a nonlinear chain constitutive behavior, which may be further developed to predict fracture (Annapooranan et al., 2022) using the approach of Mao et al. (2017) and Lamont et al. (2021), for instance. On the side of the mesogens, this theory offers a clear and practical way to incorporate well-known liquid crystal mesogen interactions via the gradient terms in Eqs. (22) – (25). Microstructural interactions such as those included in the Franck-Oseen model (Frank, 1958) could, thus, be naturally incorporated by simply adding the necessary terms to the free energy. The coupled behavior of mechanical bifurcations with phase instabilities could then be studied using more formal instability analysis such as that presented in Pampolini and Triantafyllidis (2018). While not the focus of this study, this will be important to describe mesogen patterning following an instability, for instance.

The restriction of this model to nematic systems should be addressed and discussed as a potential limitation to the current formulation. Indeed, one of the most notable features of the neo-classical theory is its natural incorporation of the order parameter Q into its foundation. In contrast, the current theory only differentiates the order of the polymer network and assumes that the mesogens maintain perfect order. Nonetheless, it is our belief that a general formulation that distinguishes between the 'order' of the polymer chains and that of the mesogens is valuable, as illustrated by the unique behavior predicted by our formulation. In the future, a statistical variance in the director orientation may be incorporated in a similar manner as the polymer network by defining $\boldsymbol{\rho}$ statistically in Eq. (6) (indeed, it is for this reason that we insist on its definition even in this formulation). We would further like to acknowledge that not all systems that are considered 'nematic' are experimentally observed to have the 'perfect' order of $Q = 1$ (where $Q = 0$ reflects an isotropic network). The general range of order for monodomain nematic elastomers may, in fact, range from 1 to values around 0.6 (see discussion in Warner and Terentjev (2007) or experimental data from Higaki et al. (2013), Urayama et al. (2009), and Tokumoto et al. (2021), for instance). It may be worth noting that these measurements are typically taken from diffraction patterns, which may not only reflect the order of the mesogens in a material with complex or hierarchical topology.

The utility of modeling these systems is ultimately in assisting the informed design of nematic elastomers with specific desired functions. We particularly note the promising applications of liquid crystal elastomers in soft robotics (Thomsen et al., 2001; Jiang et al., 2013), biomedical devices (Gao et al., 2016; Zeng et al., 2017), and, more recently, pressure-sensitive adhesives (Annapooranan et al.; Guo et al., 2023). We hope to contribute to the realization of these various applications by enabling the use of physically informed mechanical theories with practical prediction capabilities. Using the framework developed here, future studies will be dedicated to time-dependent behaviors such as relaxation (Clarke and Terentjev, 1998; Annapooranan et al.), phase transitions and instabilities (Urayama et al., 2009; Sfyris et al., 2016), and other relevant mechanical phenomena such as fracture (Annapooranan et al., 2022) and compression (Agrawal et al., 2013).

7. Acknowledgment

The author wishes to express sincere gratitude to Timothy White and Nicolas Triantafyllidis for insightful discussions that enhanced the scientific rigor and quality of this work. FJV gratefully acknowledges the support of the National Science Foundation under Award No. 2023179. The content is solely the responsibility of the authors and does not necessarily represent the official views of the National Science Foundation.

FJV and SCL acknowledge support by the Department of Energy, National Nuclear Security Administration, Predictive Science Academic Alliance Program (PSAAP) under Award Number DE-NA0003962. This report was prepared as an account of work sponsored by an agency of the United States Government. Neither the United States Government nor any agency thereof, nor any of their employees, makes any warranty, express or implied, or assumes any legal liability or responsibility for the accuracy, completeness, or usefulness of any information, apparatus, product, or process disclosed, or represents that its use would not infringe privately owned rights. Reference herein to any specific commercial product, process, or service by trade name, trademark, manufacturer, or otherwise does not necessarily constitute or imply its endorsement, recommendation, or favoring by the United States Government or any agency thereof. The views and opinions of authors expressed herein do not necessarily state or reflect those of the United States Government or any agency thereof.

8. Appendix

8.1. Derivation of the conformation tensors

We here derive the kinematic solutions for $\boldsymbol{\mu}$ and $\boldsymbol{\eta}$ in terms of the deformation gradient $\boldsymbol{F}$ and director $\boldsymbol{n}$. Recall the extension of affine polymer chain motion defined in Eq. (5) as

$$\boldsymbol{r} = \boldsymbol{F}\cdot\boldsymbol{r}_0 + \gamma\ell_0[\boldsymbol{F}\cdot\boldsymbol{n}_0 - \boldsymbol{n}]. \tag{55}$$

In the subsequent derivations, recall the shorthand notation $\langle\cdot\rangle$ as the statistical averaging operation over the conformation space Ω_r. From here, we may proceed with the derivations of $\boldsymbol{\eta}$ and $\boldsymbol{\mu}$ in terms of $\boldsymbol{F}$.

Analytical form of $\boldsymbol{\eta}$. Recall the definition of $\boldsymbol{\eta}$ defined in Eq. (6) to be:

$$\boldsymbol{\eta} = \frac{\gamma\ell_0}{r_0^2}\langle\boldsymbol{r}\otimes\boldsymbol{n}\rangle. \tag{56}$$

Using the expansion of $\boldsymbol{r}$, its definition immediately follows:

$$\begin{aligned}
\boldsymbol{\eta} &= \frac{\gamma\ell_0}{r_0^2}\langle\boldsymbol{r}\otimes\boldsymbol{n}\rangle,\\
&= \frac{\gamma\ell_0}{r_0^2}\langle\boldsymbol{F}\cdot\boldsymbol{r}_0\otimes\boldsymbol{n}\rangle + \frac{\gamma\ell_0}{r_0^2}\langle\gamma\ell_0\boldsymbol{F}\cdot\boldsymbol{n}_0\otimes\boldsymbol{n}\rangle - \frac{\gamma\ell_0}{r_0^2}\langle\gamma\ell_0\boldsymbol{n}\otimes\boldsymbol{n}\rangle,\\
&= \frac{\gamma\ell_0}{r_0^2}\boldsymbol{F}\cdot\langle\boldsymbol{r}_0\rangle\otimes\boldsymbol{n} + \frac{\gamma^2\ell_0^2}{r_0^2}\boldsymbol{F}\cdot\boldsymbol{n}_0\otimes\boldsymbol{n} - \frac{\gamma^2\ell_0^2}{r_0^2}\boldsymbol{n}\otimes\boldsymbol{n},\\
&= \chi\left[\boldsymbol{F}\cdot(\boldsymbol{n}_0\otimes\boldsymbol{n}) - \boldsymbol{\rho}\right],
\end{aligned} \tag{57}$$

where $\langle \boldsymbol{r}_0 \rangle$, which computes the first moment of P_0, is zero for a symmetric distribution.

Analytical form of $\boldsymbol{\mu}$

Recall the definition of $\boldsymbol{\mu}$ defined in Eq. (6) to be:

$$\boldsymbol{\mu} = \frac{3}{r_0^2} \langle \boldsymbol{r} \otimes \boldsymbol{r} \rangle. \tag{58}$$

Performing the substitution,

$$\begin{aligned}
\boldsymbol{\mu} &= \frac{1}{r_0^2} \langle \boldsymbol{r} \otimes \boldsymbol{r} \rangle, \\
&= \frac{1}{r_0^2} \langle [\boldsymbol{F} \cdot \boldsymbol{r}_0 + \gamma \ell_0 (\boldsymbol{F} \cdot \boldsymbol{n}_0 - \boldsymbol{n})] \otimes [\boldsymbol{F} \cdot \boldsymbol{r}_0 + \gamma \ell_0 (\boldsymbol{F} \cdot \boldsymbol{n}_0 - \boldsymbol{n})] \rangle, \\
&= \frac{1}{r_0^2} \left(\boldsymbol{F} \cdot \langle \boldsymbol{r}_0 \otimes \boldsymbol{r}_0 \rangle \cdot \boldsymbol{F}^T + 2\gamma \ell_0 \left[\boldsymbol{F} \cdot \langle \boldsymbol{r}_0 \rangle \otimes (\boldsymbol{F} \cdot \boldsymbol{n}_0 - \boldsymbol{n}) \right]_{\mathrm{S}} + 2\gamma^2 \ell_0^2 \left[(\boldsymbol{F} \cdot \boldsymbol{n}_0 - \boldsymbol{n}) \otimes (\boldsymbol{F} \cdot \boldsymbol{n}_0 - \boldsymbol{n}) \right]_{\mathrm{S}} \right), \\
&= \frac{1}{r_0^2} \left(\boldsymbol{F} \cdot \left(\langle \boldsymbol{r}_0 \otimes \boldsymbol{r}_0 \rangle + \gamma^2 \ell_0^2 \boldsymbol{n}_0 \otimes \boldsymbol{n}_0 \right) \cdot \boldsymbol{F}^T - 2\gamma^2 \ell_0^2 \left[\boldsymbol{F} \cdot \boldsymbol{n}_0 \otimes \boldsymbol{n} \right]_{\mathrm{S}} + \gamma^2 \ell_0^2 \boldsymbol{n} \otimes \boldsymbol{n} \right), \\
&= \boldsymbol{F} \cdot (\boldsymbol{\mu}_0 + \chi \boldsymbol{\rho}_0) \cdot \boldsymbol{F}^T - 2\chi \left[\boldsymbol{F} \cdot \boldsymbol{n}_0 \otimes \boldsymbol{n} \right]_{\mathrm{S}} + \chi \boldsymbol{\rho},
\end{aligned} \tag{59}$$

where the subscript $_{\mathrm{S}}$ refers to the symmetric part of a tensor (i.e., $\boldsymbol{A}_{\mathrm{S}} = (\boldsymbol{A} + \boldsymbol{A}^T)/2$). Combining the definition of $\boldsymbol{\eta}$ with the above expression and performing some basic algebra yields the form presented in Eq. (10) of the main manuscript.

8.2. Derivation of the principle of frame indifference

Let us begin by defining explicitly defining each kinematic descriptor in an arbitrarily new frame. As stated in the main text, we may consider a proper orthogonal tensor $\boldsymbol{Q}$ and an arbitrary translation vector $\boldsymbol{a}$ and write

$$\begin{aligned}
\dot{\boldsymbol{x}}^* &= \boldsymbol{Q} \cdot \dot{\boldsymbol{x}} + \dot{\boldsymbol{Q}} \cdot \boldsymbol{x} + \dot{\boldsymbol{a}}, \\
\dot{\boldsymbol{\ell}}^* &= \dot{\boldsymbol{Q}} \cdot \boldsymbol{Q}^T + \boldsymbol{Q} \cdot \boldsymbol{\ell} \cdot \boldsymbol{Q}^T, \\
\dot{\boldsymbol{n}}^* &= \boldsymbol{Q} \cdot \dot{\boldsymbol{n}} + \dot{\boldsymbol{Q}} \cdot \boldsymbol{n}, \\
\dot{\boldsymbol{\xi}}^* &= \dot{\boldsymbol{Q}} \cdot \nabla \boldsymbol{n} \cdot \boldsymbol{Q}^T + \boldsymbol{Q} \cdot \boldsymbol{\xi} \cdot \boldsymbol{Q}^T.
\end{aligned} \tag{60}$$

Using these definitions, the virtual power expenditure in the new frame is written

$$P_{int}(\mathcal{K}^*) = \int_\Omega \left[\boldsymbol{h}^* \cdot \dot{\boldsymbol{x}}^* + \boldsymbol{\sigma}^* : \boldsymbol{\ell}^* + \boldsymbol{\pi}^* \cdot \dot{\boldsymbol{n}}^* + \boldsymbol{\Sigma}^* : \boldsymbol{\xi}^* \right] dv. \tag{61}$$

Setting $P_{int}(\mathcal{K}) = P_{int}(\mathcal{K}^*)$ yields

$$\begin{aligned}
&\int_\Omega \left[\boldsymbol{h} \cdot \dot{\boldsymbol{x}} + \boldsymbol{\sigma} : \boldsymbol{\ell} + \boldsymbol{\pi} \cdot \dot{\boldsymbol{n}} + \boldsymbol{\Sigma} : \boldsymbol{\xi} \right] dv = \\
&\int_\Omega \Big[\boldsymbol{h}^* \cdot \left(\boldsymbol{Q} \cdot \dot{\boldsymbol{x}} + \dot{\boldsymbol{Q}} \cdot \boldsymbol{x} + \dot{\boldsymbol{a}} \right) + \boldsymbol{\sigma}^* : \left(\dot{\boldsymbol{Q}} \cdot \boldsymbol{Q}^T + \boldsymbol{Q} \cdot \boldsymbol{\ell} \cdot \boldsymbol{Q}^T \right) + ... \\
&... + \boldsymbol{\pi}^* \cdot \left(\boldsymbol{Q} \cdot \dot{\boldsymbol{n}} + \dot{\boldsymbol{Q}} \cdot \boldsymbol{n} \right) + \boldsymbol{\Sigma}^* : \left(\dot{\boldsymbol{Q}} \cdot \nabla \boldsymbol{n} \cdot \boldsymbol{Q}^T + \boldsymbol{Q} \cdot \boldsymbol{\xi} \cdot \boldsymbol{Q}^T \right) \Big] dv.
\end{aligned} \tag{62}$$

Combining terms,

$$\begin{aligned}
\int_\Omega \Big\{ &\dot{\boldsymbol{x}} \cdot \left[\boldsymbol{h} - \boldsymbol{Q}^T \cdot \boldsymbol{h}^* \right] + \boldsymbol{\ell} : \left[\boldsymbol{\sigma} - \boldsymbol{Q}^T \cdot \boldsymbol{\sigma}^* \cdot \boldsymbol{Q} \right] + \dot{\boldsymbol{n}} \cdot \left[\boldsymbol{\pi} - \boldsymbol{Q}^T \cdot \boldsymbol{\pi}^* \right] + \boldsymbol{\xi} : \left[\boldsymbol{\Sigma} - \boldsymbol{Q}^T \cdot \boldsymbol{\Sigma}^* \cdot \boldsymbol{Q} \right] - ... \\
&... - \boldsymbol{h}^* \cdot \left[\dot{\boldsymbol{Q}} \cdot \boldsymbol{x} + \dot{\boldsymbol{a}} \right] - \boldsymbol{\sigma}^* : \left[\dot{\boldsymbol{Q}} \cdot \boldsymbol{Q}^T \right] - \boldsymbol{\pi}^* \cdot \left[\dot{\boldsymbol{Q}} \cdot \boldsymbol{n} \right] - \boldsymbol{\Sigma}^* : \left[\dot{\boldsymbol{Q}} \cdot \nabla \boldsymbol{n} \cdot \boldsymbol{Q}^T \right] \Big\} dv = 0.
\end{aligned} \tag{63}$$

This equation must vanish at all times and for arbitrary fields of $\mathcal{K}$. We may arbitrarily set $\dot{\boldsymbol{Q}} = \boldsymbol{0}$ and, under standard variational arguments, express the resulting transformation laws:

$$\begin{aligned} \boldsymbol{h}^* &= \boldsymbol{Q} \cdot \boldsymbol{h} = \boldsymbol{0}, \\ \boldsymbol{\sigma}^* &= \boldsymbol{Q} \cdot \boldsymbol{\sigma} \cdot \boldsymbol{Q}^T \\ \boldsymbol{\pi}^* &= \boldsymbol{Q} \cdot \boldsymbol{\pi}, \\ \boldsymbol{\Sigma}^* &= \boldsymbol{Q} \cdot \boldsymbol{\Sigma} \cdot \boldsymbol{Q}^T. \end{aligned} \tag{64}$$

Note that the first equation results from the arbitrary value of $\dot{\boldsymbol{a}}$. Using these transformations, the frame indifference equation becomes

$$-\int_\Omega \boldsymbol{Q}^T \cdot \dot{\boldsymbol{Q}} : \left[\boldsymbol{\sigma} + \boldsymbol{\pi} \otimes \boldsymbol{n} + \boldsymbol{\Sigma} \cdot (\nabla \boldsymbol{n})^T\right] \, dv = 0. \tag{65}$$

Noting that $\dot{\boldsymbol{Q}}$ is a skew tensor, we may now arbitrarily set $\boldsymbol{Q} = \boldsymbol{I}$, which enforces the symmetry of the matrix in brackets. The final point-wise form of the equation is thus:

$$\boldsymbol{\sigma} + \boldsymbol{\beta} + \boldsymbol{\Sigma} \cdot (\nabla \boldsymbol{n})^T = \boldsymbol{\sigma}^T + \boldsymbol{\beta}^T + \nabla \boldsymbol{n} \cdot \boldsymbol{\Sigma}^T. \tag{66}$$

This matches the form in the main text.

8.3. Derivation of the Clausius-Duhem inequality

In this work, we propose a general energy density functional $\psi(\boldsymbol{\mu}, \boldsymbol{\rho}, \nabla \boldsymbol{n})$, which is dependent on the conformation tensors we've defined for the system. The local form of the Clausius-Duhem inequality is rewritten here:

$$\boldsymbol{\sigma} : \boldsymbol{\ell} + \boldsymbol{\pi} \cdot \dot{\boldsymbol{n}} + \boldsymbol{\Sigma} : \boldsymbol{\xi} - \dot{\psi} \geq 0. \tag{67}$$

To derive the generalized constitutive laws presented in Eqs. (23) – (25), we need to determine the evolution equations (in time) for the conformation tensors. We first note the simple relation:

$$\dot{\boldsymbol{\rho}} = \dot{\boldsymbol{n}} \otimes \boldsymbol{n} + \boldsymbol{n} \otimes \dot{\boldsymbol{n}}. \tag{68}$$

Next, we consider the evolution of $\boldsymbol{\eta}$. Taking the derivative of Eq. (11) with respect to time yields:

$$\dot{\boldsymbol{\eta}} = \chi \left[\dot{\boldsymbol{F}} \cdot (\boldsymbol{n}_0 \otimes \boldsymbol{n}) + \boldsymbol{F} \cdot (\boldsymbol{n}_0 \otimes \dot{\boldsymbol{n}}) - \dot{\boldsymbol{\rho}}\right]. \tag{69}$$

Deriving the evolution of $\boldsymbol{\mu}$ requires more steps. Let us begin by taking the time derivative without simplification:

$$\dot{\boldsymbol{\mu}} = \dot{\boldsymbol{F}} \cdot (\boldsymbol{\mu}_0 + \chi \boldsymbol{\rho}_0) \cdot \boldsymbol{F}^T + \boldsymbol{F} \cdot (\boldsymbol{\mu}_0 + \chi \boldsymbol{\rho}_0) \cdot \dot{\boldsymbol{F}}^T - \left(\dot{\boldsymbol{\eta}} + \dot{\boldsymbol{\eta}}^T\right) - \chi \dot{\boldsymbol{\rho}}. \tag{70}$$

Before proceeding, we use the relationship $\boldsymbol{\ell} = \dot{\boldsymbol{F}} \cdot \boldsymbol{F}^{-1}$ and Eq. (69) and note the following:

$$\dot{\boldsymbol{\eta}} + \dot{\boldsymbol{\eta}}^T = \boldsymbol{\ell} \cdot (\boldsymbol{\eta} + \chi \boldsymbol{\rho}) + \left(\boldsymbol{\eta}^T + \chi \boldsymbol{\rho}\right) \cdot \boldsymbol{\ell}^T + \chi \left[\boldsymbol{F} \cdot (\boldsymbol{n}_0 \otimes \dot{\boldsymbol{n}}) + (\dot{\boldsymbol{n}} \otimes \boldsymbol{n}_0) \cdot \boldsymbol{F}^T - 2\dot{\boldsymbol{\rho}}\right]. \tag{71}$$

Substituting this into Eq. (70) and combining terms:

$$\begin{aligned} \dot{\boldsymbol{\mu}} &= \boldsymbol{\ell} \cdot \left(\boldsymbol{F} \cdot (\boldsymbol{\mu}_0 + \chi \boldsymbol{\rho}_0) \cdot \boldsymbol{F}^T - \boldsymbol{\eta} - \chi \boldsymbol{\rho}\right) + \left(\boldsymbol{F} \cdot (\boldsymbol{\mu}_0 + \chi \boldsymbol{\rho}_0) \cdot \boldsymbol{F}^T - \boldsymbol{\eta}^T - \chi \boldsymbol{\rho}\right) \cdot \boldsymbol{\ell}^T \\ &\quad - \chi \left[\boldsymbol{F} \cdot (\boldsymbol{n}_0 \otimes \dot{\boldsymbol{n}}) + (\dot{\boldsymbol{n}} \otimes \boldsymbol{n}_0) \cdot \boldsymbol{F}^T - 2\dot{\boldsymbol{\rho}}\right] - \chi \dot{\boldsymbol{\rho}}, \\ &= \boldsymbol{\ell} \cdot \left(\boldsymbol{\mu} + \boldsymbol{\eta}^T\right) + (\boldsymbol{\mu} + \boldsymbol{\eta}) \cdot \boldsymbol{\ell}^T + \chi \left[\dot{\boldsymbol{n}} \otimes (\boldsymbol{n} - \boldsymbol{F} \cdot \boldsymbol{n}_0) + (\boldsymbol{n} - \boldsymbol{F} \cdot \boldsymbol{n}_0) \otimes \dot{\boldsymbol{n}}\right]. \end{aligned} \tag{72}$$

Finally, we may express the derivative of the free energy density ψ as

$$\dot{\psi} = \frac{\partial \psi}{\partial \boldsymbol{\mu}} : \dot{\boldsymbol{\mu}} + \frac{\partial \psi}{\partial \boldsymbol{\rho}} : \dot{\boldsymbol{\rho}} + \frac{\partial \psi}{\partial (\nabla \boldsymbol{n})} : \boldsymbol{\xi}. \tag{73}$$

As there are no dissipative quantities in this system, we combine the evolution equations with the Clausius-Duhem balance:

$$\begin{aligned} 0 &= \boldsymbol{\sigma} : \boldsymbol{\ell} + \boldsymbol{\pi} \cdot \dot{\boldsymbol{n}} + \boldsymbol{\Sigma} : \boldsymbol{\xi} - \left(\frac{\partial \psi}{\partial \boldsymbol{\mu}} : \dot{\boldsymbol{\mu}} + \frac{\partial \psi}{\partial \boldsymbol{\rho}} : \dot{\boldsymbol{\rho}} + \frac{\partial \psi}{\partial \left(\nabla \boldsymbol{n} \right)} : \boldsymbol{\xi} \right), \\ &= \left[\boldsymbol{\sigma} - 2 \frac{\partial \psi}{\partial \boldsymbol{\mu}} \cdot (\boldsymbol{\mu} + \boldsymbol{\eta}) \right] : \boldsymbol{\ell} + \left[\boldsymbol{\pi} + 2\chi \frac{\partial \psi}{\partial \boldsymbol{\mu}} \cdot (\boldsymbol{n} - \boldsymbol{F} \cdot \boldsymbol{n}_0) + 2 \frac{\partial \psi}{\partial \boldsymbol{\rho}} \cdot \boldsymbol{n} \right] \cdot \dot{\boldsymbol{n}} + \left[\boldsymbol{\Sigma} - \frac{\partial \psi}{\partial \left(\nabla \boldsymbol{n} \right)} \right] : \boldsymbol{\xi}. \end{aligned} \tag{74}$$

As this must vanish for arbitrary $\boldsymbol{\ell}$, $\dot{\boldsymbol{n}}$, and $\boldsymbol{\xi}$, we must enforce the terms in brackets to vanish. Thus, we arrive at the following definitions:

$$\begin{aligned} \boldsymbol{\sigma} &= 2 \left[\frac{\partial \psi}{\partial \boldsymbol{\mu}} \cdot (\boldsymbol{\mu} + \boldsymbol{\eta}) \right], \\ \boldsymbol{\pi} &= 2 \left[\chi \frac{\partial \psi}{\partial \boldsymbol{\mu}} \cdot (\boldsymbol{n} - \boldsymbol{F} \cdot \boldsymbol{n}_0) + \frac{\partial \psi}{\partial \boldsymbol{\rho}} \cdot \boldsymbol{n} \right], \\ \boldsymbol{\Sigma} &= \frac{\partial \psi}{\partial \nabla \boldsymbol{n}}. \end{aligned} \tag{75}$$

Notice that upon taking the dyadic product, $\boldsymbol{\pi} \otimes \boldsymbol{n}$, and using the definition of $\boldsymbol{\eta}$, we arrive at the general definition of the resultant stress tensor $\boldsymbol{\beta}$ given in Eq. (24).

8.4. Derivation of the fiber-reinforced neo-Hookean rubber limiting case

In the limiting case of $\kappa = 0$, we may consider that $\boldsymbol{\mu}_0 = \boldsymbol{I}$ and the director rotation is affine. As written in Eq. (45), the general solution for $\boldsymbol{n}$ is

$$\boldsymbol{n} = \frac{\boldsymbol{F} \cdot \boldsymbol{n}_0}{||\boldsymbol{F} \cdot \boldsymbol{n}_0||}. \tag{76}$$

The free energy density ψ_c of the chains in this case is simply written

$$\psi_c = \frac{G}{2} \left(\mathrm{Tr} \boldsymbol{\mu} - 3 \right). \tag{77}$$

To begin deriving the form of the free energy density in Eq. (46), let us first note the following simple identity:

$$||\boldsymbol{F} \cdot \boldsymbol{n}_0|| = \sqrt{(\boldsymbol{F} \cdot \boldsymbol{n}_0) \cdot (\boldsymbol{F} \cdot \boldsymbol{n}_0)} = \sqrt{(\boldsymbol{F}^T \cdot \boldsymbol{F}) : (\boldsymbol{n}_0 \otimes \boldsymbol{n}_0)} = \sqrt{I_4}. \tag{78}$$

Using the fact that $\boldsymbol{\mu}_0 = \boldsymbol{I}$, let us rewrite the definition of conformation tensor $\boldsymbol{\mu}$ here in a slightly different form for convenience:

$$\boldsymbol{\mu} = \boldsymbol{F} \cdot \boldsymbol{F}^T + \chi \left[\boldsymbol{F} \cdot \boldsymbol{\rho}_0 \cdot \boldsymbol{F}^T - \boldsymbol{\rho} \right] - \left(\boldsymbol{\eta} + \boldsymbol{\eta}^T \right). \tag{79}$$

Using the general solution of $\boldsymbol{n}$, we may write $\boldsymbol{\rho}$ and $\boldsymbol{\eta}$ as

$$\boldsymbol{\eta} = \chi \boldsymbol{F} \cdot (\boldsymbol{n}_0 \otimes \boldsymbol{n}_0) \cdot \boldsymbol{F}^T \left(\frac{1}{\sqrt{I_4}} - \frac{1}{I_4} \right), \qquad \boldsymbol{\rho} = \frac{1}{I_4} \boldsymbol{F} \cdot (\boldsymbol{n}_0 \otimes \boldsymbol{n}_0) \cdot \boldsymbol{F}^T. \tag{80}$$

Combining these into the definition for $\boldsymbol{\mu}$ and taking the trace,

$$\begin{aligned} \mathrm{Tr} \boldsymbol{\mu} &= \mathrm{Tr} \left(\boldsymbol{F} \cdot \boldsymbol{F}^T \right) + \chi \left[I_4 - 1 \right] - 2\chi \left(\sqrt{I_4} - 1 \right), \\ &= I_1 + \chi \left(\sqrt{I_4} - 1 \right)^2. \end{aligned} \tag{81}$$

Putting this back into the reduced form of ψ_c yields:

$$\psi_c = \frac{G}{2} \left[(I_1 - 3) + \chi \left(\sqrt{I_4} - 1 \right)^2 \right], \tag{82}$$

which matches Eq. (46) in the main text.

References

Agostiniani, V., DeSimone, A., 2012. Ogden-type energies for nematic elastomers. International Journal of Non-Linear Mechanics 47, 402–412. doi:10.1016/j.ijnonlinmec.2011.10.001.

Agrawal, A., Chipara, A.C., Shamoo, Y., Patra, P.K., Carey, B.J., Ajayan, P.M., Chapman, W.G., Verduzco, R., 2013. Dynamic self-stiffening in liquid crystal elastomers. Nature Communications 4, 1739. doi:10.1038/ncomms2772.

Anand, L., 2012. A Cahn–Hilliard-type theory for species diffusion coupled with large elastic–plastic deformations. Journal of the Mechanics and Physics of Solids 60, 1983–2002. doi:10.1016/j.jmps.2012.08.001.

Anderson, D.R., Carlson, D.E., Fried, E., 1999. A Continuum-Mechanical Theory for Nematic Elastomers. Journal of Elasticity 56, 33–58. doi:10.1023/A:1007647913363.

Annapooranan, R., Suresh Jeyakumar, S., J. Chambers, R., Long, R., Cai, S., . Ultra Rate-Dependent Pressure Sensitive Adhesives Enabled by Soft Elasticity of Liquid Crystal Elastomers. Advanced Functional Materials n/a, 2309123. doi:10.1002/adfm.202309123.

Annapooranan, R., Wang, Y., Cai, S., 2022. Highly Durable and Tough Liquid Crystal Elastomers. ACS Applied Materials & Interfaces 14, 2006–2014. doi:10.1021/acsami.1c20707.

Annapooranan, R., Wang, Y., Cai, S., 2023. Harnessing Soft Elasticity of Liquid Crystal Elastomers to Achieve Low Voltage Driven Actuation. Advanced Materials Technologies 8, 2201969. doi:10.1002/admt.202201969.

Basu, A., Wen, Q., Mao, X., Lubensky, T.C., Janmey, P.A., Yodh, A.G., 2011. Nonaffine Displacements in Flexible Polymer Networks. Macromolecules 44, 1671–1679. doi:10.1021/ma1026803.

Biggins, J.S., Terentjev, E.M., Warner, M., 2008. Semisoft elastic response of nematic elastomers to complex deformations. Physical Review E 78, 041704. doi:10.1103/PhysRevE.78.041704.

Bladon, P., Terentjev, E.M., Warner, M., 1993. Transitions and instabilities in liquid crystal elastomers. Physical Review E 47, R3838–R3840. doi:10.1103/PhysRevE.47.R3838.

Clarke, S.M., Hotta, A., Tajbakhsh, A.R., Terentjev, E.M., 2001. Effect of crosslinker geometry on equilibrium thermal and mechanical properties of nematic elastomers. Physical Review E 64, 061702. doi:10.1103/PhysRevE.64.061702.

Clarke, S.M., Terentjev, E.M., 1998. Slow Stress Relaxation in Randomly Disordered Nematic Elastomers and Gels. Physical Review Letters 81, 4436–4439. doi:10.1103/PhysRevLett.81.4436.

Conti, S., DeSimone, A., Dolzmann, G., 2002. Semisoft elasticity and director reorientation in stretched sheets of nematic elastomers. Physical Review E 66, 061710. doi:10.1103/PhysRevE.66.061710.

Dalhaimer, P., Discher, D.E., Lubensky, T.C., 2007. Crosslinked actin networks show liquid crystal elastomer behaviour, including soft-mode elasticity. Nature Physics 3, 354–360. doi:10.1038/nphys567.

Davidson, Z.S., Shahsavan, H., Aghakhani, A., Guo, Y., Hines, L., Xia, Y., Yang, S., Sitti, M., 2019. Monolithic shape-programmable dielectric liquid crystal elastomer actuators. Science Advances 5, eaay0855. doi:10.1126/sciadv.aay0855.

DeSimone, A., Dolzmann, G., 2002. Macroscopic Response of Nematic Elastomers via Relaxation of a Class of SO(3)-Invariant Energies. Archive for Rational Mechanics and Analysis 161, 181–204. doi:10.1007/s002050100174.

DeSimone, A., Teresi, L., 2009. Elastic energies for nematic elastomers. The European Physical Journal E 29, 191–204. doi:10.1140/epje/i2009-10467-9.

Ditter, D., Braun, L.B., Zentel, R., 2020. Influences of Ortho-Fluoroazobenzenes on Liquid Crystalline Phase Stability and 2D (Planar) Actuation Properties of Liquid Crystalline Elastomers. Macromolecular Chemistry and Physics 221, 1900265. doi:10.1002/macp.201900265.

Doi, M., 2013. Soft Matter Physics. Oxford University Press. doi:10.1093/acprof:oso/9780199652952.001.0001.

Eringen, A.C., 1966. Theory of Micropolar Fluids. Journal of Mathematics and Mechanics 16, 1–18.

Eringen, A.C., 1999. Microcontinuum Field Theories. 1 ed., Springer, New York.

Frank, F.C., 1958. I. Liquid crystals. On the theory of liquid crystals. Discussions of the Faraday Society 25, 19–28. doi:10.1039/DF9582500019.

Gao, Y., Mori, T., Manning, S., Zhao, Y., Nielsen, A.d., Neshat, A., Sharma, A., Mahnen, C.J., Everson, H.R., Crotty, S., Clements, R.J., Malcuit, C., Hegmann, E., 2016. Biocompatible 3D Liquid Crystal Elastomer Cell Scaffolds and Foams with Primary and Secondary Porous Architecture. ACS Macro Letters 5, 4–9. doi:10.1021/acsmacrolett.5b00729.

Germain, P., 1973. The Method of Virtual Power in Continuum Mechanics. Part 2: Microstructure. SIAM Journal on Applied Mathematics 25, 556–575. doi:10.1137/0125053.

Gil, L., Jabbour, M., Triantafyllidis, N., 2022. The Role of the Relative Fluid Velocity in an Objective Continuum Theory of Finite Strain Poroelasticity. Journal of Elasticity 150, 151–196. doi:10.1007/s10659-022-09903-6.

Guin, T., Kowalski, B.A., Rao, R., Auguste, A.D., Grabowski, C.A., Lloyd, P.F., Tondiglia, V.P., Maruyama, B., Vaia, R.A., White, T.J., 2018. Electrical Control of Shape in Voxelated Liquid Crystalline Polymer Nanocomposites. ACS Applied Materials & Interfaces 10, 1187–1194. doi:10.1021/acsami.7b13814.

Guo, H., Saed, M.O., Terentjev, E.M., 2023. Mechanism of Pressure-Sensitive Adhesion in Nematic Elastomers. Macromolecules 56, 6247–6255. doi:10.1021/acs.macromol.3c01038.

He, X., Zheng, Y., He, Q., Cai, S., 2020. Uniaxial tension of a nematic elastomer with inclined mesogens. Extreme Mechanics Letters 40, 100936. doi:10.1016/j.eml.2020.100936.

Herbert, K.M., Fowler, H.E., McCracken, J.M., Schlafmann, K.R., Koch, J.A., White, T.J., 2022. Synthesis and alignment of liquid crystalline elastomers. Nature Reviews Materials 7, 23–38. doi:10.1038/s41578-021-00359-z.

Higaki, H., Takigawa, T., Urayama, K., 2013. Nonuniform and Uniform Deformations of Stretched Nematic Elastomers. Macromolecules 46, 5223–5231. doi:10.1021/ma400771z. publisher: American Chemical Society.

Jiang, H., Li, C., Huang, X., 2013. Actuators based on liquid crystalline elastomer materials. Nanoscale 5, 5225–5240. doi:10.1039/C3NR00037K.

Lalitha Sridhar, S., Vernerey, F.J., 2020. Mechanics of transiently cross-linked nematic networks. Journal of the Mechanics and Physics of Solids 141, 104021. doi:10.1016/j.jmps.2020.104021.

Lamont, S.C., Mulderrig, J., Bouklas, N., Vernerey, F.J., 2021. Rate-Dependent Damage Mechanics of Polymer Networks with Reversible Bonds. Macromolecules 54, 10801–10813. doi:10.1021/acs.macromol.1c01943.

Mao, Y., Talamini, B., Anand, L., 2017. Rupture of polymers by chain scission. Extreme Mechanics Letters 13, 17–24. doi:10.1016/j.eml.2017.01.003.

Mao, Y., Warner, M., Terentjev, E.M., Ball, R.C., 1998. Finite extensibility effects in nematic elastomers. The Journal of Chemical Physics 108, 8743–8748. doi:10.1063/1.476303.

McCracken, J.M., Donovan, B.R., Lynch, K.M., White, T.J., 2021. Molecular Engineering of Mesogenic Constituents Within Liquid Crystalline Elastomers to Sharpen Thermotropic Actuation. Advanced Functional Materials 31, 2100564. doi:10.1002/adfm.202100564.

Mistry, D., Gleeson, H.F., 2019. Mechanical deformations of a liquid crystal elastomer at director angles between 0° and 90°: Deducing an empirical model encompassing anisotropic nonlinearity. Journal of Polymer Science Part B: Polymer Physics 57, 1367–1377. doi:10.1002/polb.24879.

Mistry, D., Traugutt, N.A., Sanborn, B., Volpe, R.H., Chatham, L.S., Zhou, R., Song, B., Yu, K., Long, K.N., Yakacki, C.M., 2021. Soft elasticity optimises dissipation in 3D-printed liquid crystal elastomers. Nature Communications 12, 6677. doi:10.1038/s41467-021-27013-0.

Pampolini, G., Triantafyllidis, N., 2018. Continuum Electromechanical Theory for Nematic Continua with Application to Freedericksz Instability. Journal of Elasticity 132, 219–242. doi:10.1007/s10659-017-9665-y.

Pei, Z., Yang, Y., Chen, Q., Terentjev, E.M., Wei, Y., Ji, Y., 2014. Mouldable liquid-crystalline elastomer actuators with exchangeable covalent bonds. Nature Materials 13, 36–41. doi:10.1038/nmat3812.

Saed, M.O., Ambulo, C.P., Kim, H., De, R., Raval, V., Searles, K., Siddiqui, D.A., Cue, J.M.O., Stefan, M.C., Shankar, M.R., Ware, T.H., 2019. Molecularly-Engineered, 4D-Printed Liquid Crystal Elastomer Actuators. Advanced Functional Materials 29, 1806412. doi:10.1002/adfm.201806412.

Saed, M.O., Gablier, A., Terentjev, E.M., 2021. Exchangeable liquid crystalline elastomers and their applications. Chemical Reviews .

Santisi d'Avila, M.P., Triantafyllidis, N., Wen, G., 2016. Localization of deformation and loss of macroscopic ellipticity in microstructured solids. Journal of the Mechanics and Physics of Solids 97, 275–298. doi:10.1016/j.jmps.2016.07.009.

Schlafmann, K.R., Alahmed, M.S., Lewis, K.L., White, T.J., . Large Range Thermochromism in Liquid Crystalline Elastomers Prepared with Intra-Mesogenic Supramolecular Bonds. Advanced Functional Materials n/a, 2305818. doi:10.1002/adfm.202305818.

Sfyris, G.I., Danas, K., Wen, G., Triantafyllidis, N., 2016. Freedericksz instability for the twisted nematic device: A three-dimensional analysis. Physical Review E 94, 012704. doi:10.1103/PhysRevE.94.012704.

Shaha, R.K., Merkel, D.R., Anderson, M.P., Devereaux, E.J., Patel, R.R., Torbati, A.H., Willett, N., Yakacki, C.M., Frick, C.P., 2020. Biocompatible liquid-crystal elastomers mimic the intervertebral disc. Journal of the Mechanical Behavior of Biomedical Materials 107. doi:10.1016/j.jmbbm.2020.103757.

Spencer, A.J., 1985. Continuum theory of the mechanics of fibre-reinforced composites. Springer.

Thomsen, D.L., Keller, P., Naciri, J., Pink, R., Jeon, H., Shenoy, D., Ratna, B.R., 2001. Liquid Crystal Elastomers with Mechanical Properties of a Muscle. Macromolecules 34, 5868–5875. doi:10.1021/ma001639q.

Tokumoto, H., Zhou, H., Takebe, A., Kamitani, K., Kojio, K., Takahara, A., Bhattacharya, K., Urayama, K., 2021. Probing the in-plane liquid-like behavior of liquid crystal elastomers. Science Advances 7, eabe9495. doi:10.1126/sciadv.abe9495.

Urayama, K., Kohmon, E., Kojima, M., Takigawa, T., 2009. Polydomain-Monodomain Transition of Randomly Disordered Nematic Elastomers with Different Cross-Linking Histories. Macromolecules 42, 4084–4089. doi:10.1021/ma9004692.

Vernerey, F.J., 2018. Transient response of nonlinear polymer networks: A kinetic theory. Journal of the Mechanics and Physics of Solids 115, 230–247.

Vernerey, F.J., 2022. Mechanics of transient semi-flexible networks: Soft-elasticity, stress relaxation and remodeling. Journal of the Mechanics and Physics of Solids 160, 104776. doi:10.1016/j.jmps.2022.104776.

Vernerey, F.J., Long, R., Brighenti, R., 2017. A statistically-based continuum theory for polymers with transient networks. Journal of the Mechanics and Physics of Solids 107, 1–20.

Verwey, G.C., Warner, M., 1997. Compositional Fluctuations and Semisoftness in Nematic Elastomers. Macromolecules 30, 4189–4195. doi:10.1021/ma961801i. publisher: American Chemical Society.

Wang, Z., El Hajj Chehade, A., Govindjee, S., Nguyen, T.D., 2022. A nonlinear viscoelasticity theory for nematic liquid crystal elastomers. Journal of the Mechanics and Physics of Solids 163, 104829. doi:10.1016/j.jmps.2022.104829.

Wang, Z., Wang, Z., Zheng, Y., He, Q., Wang, Y., Cai, S., 2020. Three-dimensional printing of functionally graded liquid crystal elastomer. Science Advances 6, eabc0034. doi:10.1126/sciadv.abc0034.

Warner, M., Terentjev, E., 2007. Liquid Crystal Elastomers. International Series of Monographs on Physics, OUP Oxford.

Xu, L., Zhu, C., Lamont, S.C., Zou, X., Yang, Y., Chen, S., Ding, J., Vernerey, F.J., 2024. Programming motion into materials using electricity-driven liquid crystal elastomer actuators. Soft Robotics (in press) .

Zeng, H., Wani, O.M., Wasylczyk, P., Kaczmarek, R., Priimagi, A., 2017. Self-Regulating Iris Based on Light-Actuated Liquid Crystal Elastomer. Advanced Materials 29, 1701814. doi:10.1002/adma.201701814.

Zhang, Y., Xuan, C., Jiang, Y., Huo, Y., 2019. Continuum mechanical modeling of liquid crystal elastomers as dissipative ordered solids. Journal of the Mechanics and Physics of Solids 126, 285–303. doi:10.1016/j.jmps.2019.02.018.